Angular Radon Spectrum for Rotation Estimation

Angular Radon Spectrum for Rotation Estimation

Dario Lodi Rizzinie

PII: S0031-3203(18)30250-4
DOI: 10.1016/j.patcog.2018.07.017
Reference: PR 6609

To appear in: *Pattern Recognition*

Received date: 12 June 2017
Revised date: 31 May 2018
Accepted date: 10 July 2018

Please cite this article as: Dario Lodi Rizzinie, Angular Radon Spectrum for Rotation Estimation, *Pattern Recognition* (2018), doi: 10.1016/j.patcog.2018.07.017

Highlights

- Formal definition and derivation of Angular Randon Spectrum (ARS).
- Estimation of point set rotation through efficient computation of ARS.
- Experimental assessment of rotation accuracy on benchmark datasets.

Angular Radon Spectrum for Rotation Estimation

Dario Lodi Rizzini[1]

Department of Engineering and Architecture, University of Parma,
Parco Area delle Scienze 181A, 43124 Parma, Italy

Abstract

This paper presents a robust method for rotation estimation of planar point sets using the Angular Radon Spectrum (ARS). Given a Gaussian Mixture Model (GMM) representing the point distribution, the ARS is a continuous function derived from the Radon Transform of such distribution. The ARS characterizes the orientation of a point distribution by measuring its alignment w.r.t. a pencil of parallel lines. By exploting its translation and angular-shift invariance, the rotation angle between two point sets can be estimated through the correlation of the corresponding spectra. Beside its definition, the novel contributions of this paper include the efficient computation of the ARS and of the correlation function through their Fourier expansion, and a new algorithm for assessing the rotation between two point sets. Moreover, experiments with standard benchmark datasets assess the performance of the proposed algorithm and other state-of-the-art methods in presence of noisy and incomplete data.

Keywords: Rotation estimation, Gaussian Mixture Models

1. Introduction

An important operation in perception and pattern recognition is the estimation of the rigid transformation between two point sets representing the same object or scene from different viewpoints. Registration is a primitive for a wide range of applications including localization and mapping [1, 2, 3], shape

[1]E-mail: dario.lodirizzini@unipr.it

matching [4, 5, 6] and medical image processing [7]. The different views of the same object or scene usually differ in both the relative orientation and position. In the most popular approach to registration, the rigid transformation is generally solved as a whole, once the corresponding parts between the two views or objects have been found. The correspondence-based methods [8, 9, 10, 11, 12, 13, 14, 15, 16], which search the rigid transformation by minimizing the distances between corresponding points in the two compared point sets, belong to this category. Such algorithms require an initial guess of the rigid transformation between the two sets in order to establish the associations, and iteratively refine its value. The initial guess is either provided by the specific context of the problem (e.g. a measurement like the odometry of a robot or a vehicle) or by another correspondence-less method. These methods are strongly affected by wrong correspondences between the matching parts of the observations. Recently, robust associations techniques [17, 13, 15, 18] have been proposed to detect consistent associations and filter outliers associations, but they may fail when the initial correspondence set is inaccurate.

A second category of methods includes the registration algorithms that compare feature sets, histograms or functions extracted from each point set. The choice of the features or histograms depends on the specific application: for example spherical harmonics [19, 20, 21, 22, 23] are often used for the registration of 3D polygon meshes or point clouds, whereas log-polar transform and phase correlation [24, 25, 26] are applied for images. Many of these techniques decouple the estimation of rotation and translation into two different steps, and implicitly assume that their description of orientation is not affected by translation. Thus, pose estimation can be solved by separately addressing rotation and translation. Given a descriptor based on strong property of point sets, such decomposition enables robust solution of orientation estimation. However, such decoupling just an approximation for the aforementioned methods, since angular measurements are referred to a privileged reference point like the object centroid or the image center. For example, the polar coordinates of spherical harmonics are relative to the center of a polygon mesh, or the log-polar mapping used in

image registration is computed w.r.t. the image center. Collinearity [27, 28] is possibly the simplest property observable in a set of points that is really invariant to rigid transformation. While the equation of a line through a group of aligned points changes with translation, the orientation of a pencil of parallel line is invariant to translation. Moreover, the relative orientation between line pencils is invariant to rotation (angular-shift invariance). Methods based on *Hough Spectrum* (HS) [29, 30] exploit this property to *exactly* decouple rotation and translation. The HS is an angular histogram derived from Hough Transform (HT) [31] that detects point alignments to a pencil of parallel lines instead of a single line. Rotation angle corresponds to the angular shift that maximizes the correlation of two spectra. Although effective, HS inherits the main shortcomings of HT like the curse of discretization of continuous quantities, the recourse to brute-force operations on histograms, and the formally incomplete modelling of data uncertainty.

In this paper, we propose a novel method for estimating rotation between planar point sets using the *Angular Radon Spectrum* (ARS). Since points are usually acquired from noisy measurements of objects or scenes, a Gaussian mixture model (GMM) consisting of isotropic and identical kernels [32, 33, 34] is adopted to represent each input point distribution. In analogy with HS, ARS is a continuous function derived from the Radon Transform (RT) [35, 36] of a GMM. Similarly to RT in respect to HT [37], ARS provides a sound mathematical basis for HS and measures the point density along each pencil of lines. The ARS of a point set characterizes the orientation according to the collinearity of its points, and is invariant to translation. Given two point sets related by an isometry, the correlation of their spectra enables the robust evaluation of rotation. The rotation angle is estimated by searching the global maximum of the correlation function. If there are several maxima, there are multiple rotation angles candidates. Thus, our method is a global algorithm that does not require an initial estimate. Figure 1 shows the ARS computed for two different point sets and the application of their correlation function to the estimation of the rotation angle. In summary, the contributions of this works are the following.

1. We provide the formal definition of the ARS and the derivation of its expression for identical and isotropic GMMs.
2. We derive the Fourier series of the ARS for efficient approximation and prove a bound on the approximation error of the truncated series.
3. We provide a closed-form expression of the ARS correlation function and its application to the estimation of rotation.

Experiments illustrate the accuracy and robustness of the proposed ARS-based method as compared to the HS and other algorithms, when applied to rotation estimation with noisy and missing data.

This paper is organized as follows. Section 2 reviews existing methods for pose and rotation estimation. Section 3 defines the general definitions and provides the RT of a GMM representing a point set. Section 4 illustrates the ARS and its efficient computation using its Fourier series expansion. Section 5 presents the algorithm based on ARS for evaluating rotation. Section 6 shows experimental results on standard datasets. Finally, Section 7 gives the concluding remarks.

2. Related Work

The literature on registration is large and includes different formulations for several (sometimes loosely) related problems. The differences among the approaches depend on the type and domain of input data (images, polygon meshes, 2D or 3D point clouds, laser scans, etc.) and on the specific problem statement (availability of initial guess, joint evaluation of rotation and translation, etc.). The common goal is the estimation of the relative pose or orientation between two views of the same object or scene. While the focus of the present work is on rotation estimation, the survey presented in this section also includes the registration methods that cannot decouple rotation and translation, and the shape recognition algorithms assessing rigid transformation only to remove spatial bias. As discussed in section 1, a general rough classification criterion divides registration methods into correspondence-based and correspondence-less.

Iterative Closest Point (ICP) [8] is perhaps the most popular registration algorithm that iteratively refines the transformation by matching each point of the source point set with its closest point in the target set. Over the years, several variants like ICP with soft asssignment [38], ICP with surface matching [10], affine ICP [12] have been proposed. The critical step of ICP is the search for correct matches between points, whereas the computation of the best rigid transformation is a solved problem both for 2D and 3D cases [39]. Generalized Procrustes Analysis (GPA) has also been proposed to simultaneously register multiple point sets in a single optimization step [40, 41]. Biber and Strasser [9] propose the Normal Distributions Transform (NDT) to model the probability of measuring a point as a mixture of normal distributions. NDT substitutes the hard point association with a soft association and estimates the transformation by maximizing the probability function. The approach has been extended to 3D point clouds [11] and, with ICP, is part of standard registration techniques [14]. The NDT techniques is implicitly related to several registration techniques [42, 34, 6] matching GMMs computed on point sets.

Several techniques have been developed to estimate robust and consistent associations, which usually operate in two steps. In the first step, an initial set of putative associations is estimated according to similarity (e.g. feature descriptors) or geometric criteria (e.g. nearest-neighbor search). Since the putative associations often include both correct matches and and outliers, the second step filters outliers using strong consistency constraints. The most popular algorithm belonging to this approach is RANSAC [43] and its many variants like MLESAC [44]. Other techniques have been proposed to address non-rigid registration problem or the case with non-parametric consistency constraints. Coherence point drift (CPD) algorithm [17] represents point sets with a GMM and discriminates outliers by forcing GMM centroids to move coherently as a group. Alternatively, Ma et al. [13] proposed Vector Field Consensus (VFC) to compute consistent associations. This method solve correspondences by interpolating a vector field between the two point sets. The search of consistent association has been also extended to the non-rigid registration of shapes

represented as GMMs [15, 16]. The hypothesize-and-verify approach is often successful in the estimation of associations, but it depends on the initial evaluation of putative correspondences. When no similarity criterion is available, For this reason, correspondence-based algorithms are often considered techniques for refining the estimation.

In the correspondence-less approach, the separation of rotation and translation estimation is more common. Depending on the specific input data, such algorithms may describe orientation in term of features, histograms or other characteristic functions. The rotation between the source and the target objects is computed by matching such features, or by correlating histograms and functions. The assessment of translation is often solved, once the rotation has been assessed. PCA-based techniques [45] find the principal axes of the two point sets and find the rotation that aligns them. Since they are rather sensitive to missing data, noise, variations in density and lack of pronounced directions, PCA-based techniques are suitable only for artificial and complete models of objects. The PCA-based method presented in [46] estimates the relative pose of 3D objects from their 2D images without searching correspondences. Images are mapped to an ideal 3D sphere and their correlation is computed using spherical harmonic expansion. Other methods are designed for organized data like contour curves or polygon meshes. Latecki et al. [4, 5] proposed a shape similarity metric for comparing two planar closed curves representing the contours of two objects. The estimation of orientation is an indirect result of removing the orientation bias between the tangent histograms. Spherical harmonic expansion is a popular approach originally applied to 3D polygon meshes [19, 23]. To obtain spherical harmonic decomposition, each point of the object surface must be mapped to the unit sphere. Makadia et al. [20] use spherical harmonic expansion to find the rotation between 3D point clouds. The polar parameterization, which is not available like in the case of polygon meshes, is built using surface orientation histograms computed from the original range measurements. The same approach has been applied to the registration of spherical images [21].

The literature on image registration mainly consists of correspondence-less

methods. Image structure is regularly organized as a spatial matrix of regularly sampled data. Therefore, Fourier analysis and phase correlation techniques [47] have been applied to the estimation of rotation and translation. Rotation and translation jointly affect the image spectra, but these transformation are approximatively computed into two consecutive steps. Log-polar transform [48, 49] has been used to attenuate such dependence. In particular, log-polar transform enables rotation estimation by correlating the logarithmic modules of two image spectra. Then, phase correlation provides an estimation of translation according to Fourier phase-shift theorem [48]. The application of a logarithmic map facilitates the comparison of images with large differences in scale, since scale coefficient becomes an addititive term [49]. The enhanced correlation coefficient (ECC) [25] is a general method for computing the transformation parameters that minimize the difference between two images. The algorithm in [34] performs registration by representing 3D point sets with GMMs.

Recently, the method based on the HS has been proposed for 2D rotation estimation [29] and, then, extended to 3D problems [30]. It has been used to merge local maps [1, 2] or to detect the dominant orientation in a laser scan [50]. Informally, the HS detects dominant pencils of parallel lines in a point set and is translation-invariant and angular-shift invariant. The main limitations of this algorithm are due to the parameter space discretization. Beside requiring the arbitrary definition of cell size, the combined effect of discretization and translation introduces deformation and loss of information in the spectrum [29]. Moreover, many operations on discrete sets like histogram correlation are often performed through brute-force computation.

3. The Radon Transform of a Gaussian Mixture Model

Let $\mathcal{P} = \{\mu_i\}_{i=1,\dots,n_p}$ with $\mu_i \in \mathbb{R}^2$ be the estimated position vectors of the points. It is convenient to define the *density function* $f : \mathbb{R}^2 \to \mathbb{R}_0^+$ that represents the point density in the plane and is proportional to the probability density function (PDF) of finding a point. The integral of $f(\cdot)$ on the whole

plane $\mathbb{R}^2$ is equal to the number of points $|\mathcal{P}| = n_p$. If the point positions are exactly known, then the density function consists of Dirac impulse distributions, i.e. $f(r) = \sum_{i=1}^{n_p} \delta(r - \mu_i)$. However, in most problems the point coordinates are estimated with a given uncertainty and the function $f(r)$ should represent a looser concentration around the input points. The GMM [32] is a widely used model in kernel density estimation and other machine learning applications. According to this model, each point is associated to a Gaussian kernel $\mathcal{N}(\mu_i, \Sigma_i)$ centered on μ_i and with covariance matrix Σ_i. Assuming that all the kernels have equal probability, the resulting density function has equation

$$f(r) = \sum_{i=1}^{n_p} g_i(r) = \sum_{i=1}^{n_p} \frac{1}{2\pi|\Sigma_i|^{1/2}} \exp\left(-\frac{1}{2}\|r - \mu_i\|^2_{\Sigma_i}\right) \tag{1}$$
$$\|r - \mu_i\|^2_{\Sigma_i} = (r - \mu_i)^\top \Sigma_i^{-1} (r - \mu_i)$$

As discussed above, the probability density function is obtained by multiplying $f(r)$ by the factor $1/n_p$. A common hypothesis is that the Gaussian kernels are *identical* and *isotropic*, i.e. $\Sigma_i = \sigma I_2$ for $i = 1, \ldots, n_p$. Figure 2(a) shows an example of an isotropic and identical GMM. This assumption is satisfied for several real applications, enables analytically elegant results, and is implicitly adopted in the rest of the paper, unless otherwise stated.

Given a point distribution model, the goal is to measure the alignment of the point set w.r.t. a line. The *Radon Transform* (RT) [35] is a functional that associates a function $f(\cdot)$ with values in $\mathbb{R}^d$ to its integral over a $d-1$ dimension manifold $\mathcal{F}_q \subset \mathbb{R}^d$ with parameter q. The manifold $\mathcal{F}_q$ is defined by a specific parameter vector $q \in \mathcal{Q}$, where $\mathcal{Q}$ is the parameter space. If $f(\cdot)$ is a density function as in eq. (1) and $\mathcal{F}_q$ is a line, the RT measures the density of the points aligned on the line with parameter q. RT could be considered the continuous version of the Hough Transform [51], which has been extensively used to fit lines and other general curves. The general definition of RT is the following.

Definition 1. *Let $f : \mathbb{R}^d \to \mathbb{R}$ be a function, $q \in \mathcal{Q}$ a parameter vector, $\mathcal{F}_q =$*

$\{r \in \mathbb{R}^d : h(r, q) = 0\}$ *a* $d-1$ *dimension manifold. The* Radon Transform *(RT) of* $f(\cdot)$ *is a function defined as*

$$\mathcal{R}[f](q) = \int_{\mathbb{R}^d} f(r)\ \delta(h(r, q))\ dr \tag{2}$$

An important case is the RT defined for $(d-1)$-dimension hyperplanes $h(r, q) = \xi^\top r - \rho$, where ξ and ρ are the parameters of Hessian normal form. In particular, for the planar case ($d = 2$) the parameter vector is $q = [\theta, \rho]^\top$, $\xi(\theta) = [\cos\theta, \sin\theta]^\top$ and $\mathcal{F}_q$ corresponds to a line. Unit vector $\xi(\theta)$ depends on the angle θ, but the dependence on the angle will be omitted when it is clear from the context. In this case, the parameter space $\mathcal{Q}$ can be chosen as either $[0, \pi[\times\mathbb{R}$ or $[0, 2\pi[\times\mathbb{R}_0^+$ in order to avoid the double representation of the same line [29]. In this work, we adopt the first choice of parameter domain, i.e. $\mathcal{Q} = [0, \pi[\times\mathbb{R}$, for both efficiency and analytical convenience. A point $r \in \mathbb{R}^2$ can be expressed w.r.t. the orthogonal basis $[\xi, \xi']$ as $r = \rho\xi + s\xi'$, where $\xi'(\theta) = [-\sin\theta, \cos\theta]^\top$ and $\rho, s \in \mathbb{R}$. The argument of ξ' is omitted as well. Thus, the integral of equation (2) can be rewritten as

$$\mathcal{R}[f](\theta, \rho) = \int_{-\infty}^{\infty} f(\rho\xi + s\xi')\ ds \tag{3}$$

Our goal is to measure the alignment of a point set represented by a GMM w.r.t. a given line using the RT. The Radon Transform of a GMM (GMM-RT) can be computed from the RT of a Gaussian probability density function. The following result provides the solution.

Proposition 1. *Let* $g_i(\cdot)$ *be the the PDF of a normally distributed point* $r \sim \mathcal{N}(\mu_i, \Sigma_i)$, $q = [\theta, \rho]^\top$ *be the Hessian parameters of a line,* ξ *and* ξ' *be defined as in eq. (3). Then,*

$$\mathcal{R}[g_i](\theta, \rho) = \frac{1}{\sqrt{(2\ \pi)a|\Sigma_i|}} \exp\left(\frac{b^2 - ac}{2a}\right) \tag{4}$$

where $a = \xi'^\top\Sigma_i^{-1}\xi'$, $b = \xi'^\top\Sigma_i^{-1}(\rho\xi - \mu_i)$ *and* $c = (\rho\xi - \mu_i)^\top\Sigma_i^{-1}(\rho\xi - \mu_i)$.

Proof 1. *A generic point* r *of the line* q *can be parameterized as* $r = t\xi + \rho\xi'$

and its coordinate values are

$$\begin{aligned}\|r-\mu_i\|^2_{\Sigma_i} &= (s\xi' + \rho\xi - \mu_i)^\top \Sigma_i^{-1}(s\xi' + \rho\xi - \mu_i) \\ &= \underbrace{(\xi'^\top \Sigma_i^{-1}\xi')}_{a}\ s^2 + 2\underbrace{(\xi'^\top \Sigma_i^{-1}u)}_{b}\ s + \underbrace{(u^\top \Sigma_i^{-1}u)}_{c} \\ &= a\left(s+\frac{b}{a}\right)^2 - \frac{b^2}{a} + c \end{aligned} \tag{5}$$

where $u = \rho\xi - \mu_i$. Hence, it can be substituted into the argument of Gaussian PDF $g_i(\cdot)$ and used to compute RT as in eq. (3).

$$\begin{aligned}\mathcal{R}[g_i](q) &= \frac{1}{2\ \pi\sqrt{|\Sigma_i|}} \int_{-\infty}^{+\infty} \exp\left(-\frac{a}{2}\left(s+\frac{b}{a}\right)^2 + \frac{b^2}{2a} - \frac{c}{2}\right) ds \\ &= \frac{\exp\left(\frac{b^2-ac}{2a}\right)}{\sqrt{(2\ \pi)^2|\Sigma_i|}} \int_{-\infty}^{+\infty} \exp\left(-\frac{a}{2}p^2\right) dp \\ &= \frac{1}{\sqrt{(2\ \pi)^2|\Sigma_i|}}\ \sqrt{\frac{2\pi}{a}}\ \exp\left(\frac{b^2-ac}{2a}\right)\end{aligned}$$

In the above expression the integration parameter s is substituted by $p = s + b/a$.

Proposition 1 provides the general form of the RT of a normal distribution. The GMM-RT in eq. (1) is equal to the sum of terms in the equation (4). If all the normal kernels of the GMM are isotropic, i.e. $\Sigma_i = \sigma_i^2 I_2$ for each i, the RT expression is considerably simpler. In particular, the analytical expression is

$$\mathcal{R}[f](\theta,\rho) = \sum_{i=1}^{n_p} \frac{1}{\sqrt{2\pi}\sigma_i} \exp\left(-\frac{(\rho - \xi^\top \mu_i)^2}{2\sigma_i^2}\right) \tag{6}$$

Note that, since the hypothesis of identical kernel is not used yet, the values of standard deviations σ_i may be different. Figure 2(b) illustrates the level set plot of a GMM-RT. The sinusoidal components corresponding to lines are visible. Given a direction θ, the RT of a PDF can be interpreted as a marginalization of the joint distribution of t and ρ, where t is the marginalized random variable. Thus, $\mathcal{R}[f](\theta,\rho)$ is proportional to the density function of line parameter ρ.

4. Angular Radon Spectrum

In this section, we introduce *Angular Radon Spectrum* (ARS) for measuring the importance of a specific direction in a point set. An important property of

the ARS is its rotation invariance, that will be fully exploited in next section. Since the computation of the ARS of a point set is computationally expensive, we also propose an efficient approximation.

4.1. Definition of Angular Radon Spectrum

Given a point set represented by a GMM, the maxima of the related GMM-RT correspond to the lines passing through high point density regions. Like its discrete equivalent, the Hough Transform, the RT enables the efficient search of the alignments, which are subsets of points lying on the same line. However, the goal of this work is the estimation of rotation, which is related to the global orientation of the whole point set. Geometrically, while alignment is associated to the concentration of point density on a single line with parameters $q = [\theta, \rho]^\top$, the importance of an orientation depends on the density concentration on a pencil of parallel lines with parameter θ. The approach followed here is similar to the one adopted in the derivation of Hough Spectrum from Hough Transform [29]. The main difference is that the formulation is obtained by manipulating continuous functions instead of histograms. The following definition addresses these issues.

Definition 2. *Let $f : \mathbb{R}^2 \to \mathbb{R}_0^+$ be a non-negative function, $\mathcal{R}[f](\cdot)$ the RT with line parameters $q = [\theta, \rho]^\top$. Then, the* Angular Radon Spectrum *(ARS) is a functional defined as*

$$\mathcal{S}_\kappa [f] (\theta) = \int_{-\infty}^{+\infty} \kappa \left(\mathcal{R}[f](\theta, \rho) \right) d\rho \tag{7}$$

where $\kappa : \mathbb{R}_0^+ \to \mathbb{R}_0^+$ is strictly superadditive, i.e. $\kappa(x + y) > \kappa(x) + \kappa(y)$, $0 < x \leqslant y$.

The ARS has been defined only for non-negative functions like the GMM in order to limit the domain of concentration function $\kappa(\cdot)$. Although this restriction could be removed without formally affecting the definition, the geometric interpretation of the ARS is less clear for functions with negative values. Moreover, the only condition on $\kappa(\cdot)$ is strict superadditivity. Strict superadditivity

is required in order to highlight the density concentration. If only simple superadditivity holds, i.e. $\kappa(x+y) \geqslant \kappa(x) + \kappa(y)$, the resulting ARS may not properly discriminate. For example, when $\kappa(x) = x$, the ARS of the GMM in eq. (1) is constant, since the integral of the Gaussian-like functions of GMM-RT in eq. (6) is equal to 1. Following the suggestion in [29], the function $\kappa(x) = x^2$ is implicitly used in the remaining of the paper.

Proposition 2. *Let $f(\cdot)$ be an isotropic GMM defined as in eq. (1) with $\Sigma_i = \sigma_i^2 I_2$ and $\kappa(x) = x^2$ be an accumulation function. Then, the ARS of an isotropic GMM is equal to*

$$\mathcal{S}_\kappa\left[f\right](\theta) = \sum_{i=1}^{n_p-1} \sum_{j=i+1}^{n_p} \beta_{ij} \exp\left(-\frac{(\xi^\top(\mu_i - \mu_j))^2}{\sigma_i^2 + \sigma_j^2}\right) + \sum_{i=1}^{n_p} \alpha_i \tag{8}$$

where $\alpha_i = \frac{1}{2\sqrt{\pi}\sigma_i}$ and $\beta_{ij} = \sqrt{\frac{2}{\pi(\sigma_i^2+\sigma_j^2)}}$.

Proof 2. *The GMM-ARS is obtained by integrating the square of the GMM-RT in equation (6):*

$$\begin{aligned}\mathcal{R}[f](\theta,\rho)^2 =& \sum_{i=1}^{n_p} \frac{1}{2\pi\sigma_i^2} \underbrace{\exp\left(-\frac{(\rho - \xi^\top\mu_i)^2}{\sigma_i^2}\right)}_{A_i} \\ +2 & \sum_{i=1}^{n_p-1} \sum_{j=i+1}^{n_p} \frac{1}{2\pi\sigma_i\sigma_j} \underbrace{\exp\left(-\frac{(\xi^\top\mu_i - \rho)^2}{2\sigma_i^2} - \frac{(\xi^\top\mu_j - \rho)^2}{2\sigma_j^2}\right)}_{B_{ij}}\end{aligned} \tag{9}$$

The integral of eq. (9) w.r.t. ρ is obtained by integrating separately the terms A_i and B_{ij}. The integral of the Gaussian function A_i over variable ρ is equal to $\sigma_i\sqrt{\pi}$. The term B_{ij} is the product of two Gaussian PDFs $\mathcal{N}_\rho(\xi^\top\mu_i, \sigma_i^2)$ and $\mathcal{N}_\rho(\xi^\top\mu_j, \sigma_j^2)$ and can be re-written as [52, sec. 8.1.8, p. 42]

$$\begin{aligned} B_{ij} &= \exp\left(-\frac{(\xi^\top\mu_i - \xi^\top\mu_j)^2}{\sigma_i^2 + \sigma_j^2}\right) \exp\left(-\frac{(\rho - \mu_c)^2}{2\sigma_c^2}\right) \\ \mu_c &= \frac{\sigma_j^2\ (\xi^\top\mu_i) + \sigma_i^2\ (\xi^\top\mu_j)}{\sigma_i^2 + \sigma_j^2} \qquad \sigma_c^2 = \frac{\sigma_i^2\sigma_j^2}{\sigma_i^2 + \sigma_j^2} \end{aligned} \tag{10}$$

The integral of B_{ij} w.r.t. ρ is equal to

$$\int_{-\infty}^{+\infty} B_{ij}\, d\rho = \exp\left(-\frac{(\xi^\top\mu_i - \xi^\top\mu_j)^2}{\sigma_i^2 + \sigma_j^2}\right) \sqrt{\frac{2\pi\sigma_i^2\sigma_j^2}{\sigma_i^2 + \sigma_j^2}} \tag{11}$$

Equation (8) follows from the substitution of the integrals of A_i and B_{ij}.

The analytical expression of GMM-ARS is rather simple if all the normal kernels of the mixture are identical, i.e. all $\sigma_i = \sigma$. In this case, $\alpha_i = 1/(2\sigma\sqrt{\pi})$ and $\beta_{ij} = 1/(\sigma\sqrt{\pi})$ for $i, j = 1, \ldots, n_p$ For the remaining of the paper, we assume that the GMM kernels are identical and that the GMM-ARS is

$$\mathcal{S}_\kappa [f](\theta) = \frac{1}{\sigma\sqrt{\pi}} \sum_{i=1}^{n_p-1} \sum_{j=i+1}^{n_p} \psi_{ij}(\theta) + \frac{n_p}{2\sigma\sqrt{\pi}} \tag{12}$$

$$\psi_{ij}(\theta) = \exp\left(-\left(\frac{\xi^\top(\mu_i - \mu_j)}{2\sigma}\right)^2\right) \tag{13}$$

The GMM-ARS consists of a sum of $n_p(n_p-1)/2$ kernel functions $\psi_{ij}(\theta)$. Thus, the computation complexity of its evaluation for one value of θ is quadratic with respect to the number of points. An efficient approximation will be presented in the following section.

Each kernel function $\psi_{ij}(\theta)$ measures the likelihood that the point pairs with indices i and j lies on a line with parameter θ. The image of $\psi_{ij}(\theta)$ is the interval $[e^{-(\|\mu_i-\mu_j\|/2\sigma)^2}, 1]$, where the maximum is achieved when $\xi(\theta)$ is orthogonal to vector $\mu_i - \mu_j$ and the minimum when it is parallel. Observe that the span between the minimum and the maximum of kernel increases with the distance between μ_i and μ_j, and decreases with the standard deviation σ. A larger span means greater discrimination capability in detection of a dominant orientation θ. From a geometric perspective, the GMM-ARS counts the point pairs oriented according to the pencil of lines with a given parameters θ. Thus, the straightforward application of the ARS is the search of the dominant directions in a point set. There is another application that derives from an important property of the ARS that is stated in the following.

Proposition 3 (Translation invariance and Rotation shift-invariance). *Let $f(r)$ and $\mathcal{S}_\kappa[f](\theta)$ be respectively the density function and the ARS of a point set, and $\bar{f}(r) = f(R(\delta)r + t)$ be the transformed density function where $t \in \mathbb{R}^2$*

is the translation vector and $R(\delta)$ the rotation matrix for angle $\delta \in S^1$. Then,

$$\mathcal{S}_\kappa \left[\bar{f}\right](\theta) = \mathcal{S}_\kappa [f](\theta + \delta) \tag{14}$$

Proof 3. *The transformed point is written as*

$$R(\delta)r + t = (\rho + t^\top \bar{\xi})\bar{\xi} + (s + t^\top \bar{\xi}')\bar{\xi}' = \bar{\rho}\bar{\xi} + \bar{s}\bar{\xi}' \tag{15}$$

where $\bar{\xi} = R(\delta)\xi = \xi(\theta+\delta)$ and $\bar{\xi}' = R(\delta)\xi' = \xi'(\theta+\delta)$. The RT is computed by solving the integral in eq. (3) after the integration variable change with $\bar{s}$. The integration domain is the same. The RT is s.t. $\mathcal{R}\left[\bar{f}\right](\theta, \rho) = \mathcal{R}[f](\theta+\delta, \rho+t^\top\bar{\xi})$. Similarly, the integration of eq. (7) is solved w.r.t. the changed integration variable $\bar{\rho}$. The result follows.

The translation invariance and the angular shift caused by rotation are general properties of the ARS, which can be easily verified by direct substitution in the GMM-ARS expression of eq. (12). These properties enable the comparison of different point sets observed from different viewpoints. In particular, since ARS is translation invariant, the estimation of rotation between two point sets can be achieved comparing the two respective ARS. Stated differently, the spectrum enables the decoupling of rotation and translation. This issue will be addressed in section 5.

4.2. Efficient Evaluation of Radon Spectrum

In the previous section, we observed that the computational complexity of the ARS evaluation for a given value of θ is quadratic. The complexity depends on the number of kernel functions $\psi_{ij}(\theta)$, which in turn is equal to the number of point pairs. While the quadratic complexity is unavoidable due to the intrinsic ARS definition, the demanding operation is performed during the initialization. The argument of the kernel function in eq. (13) can be rewritten as

$$\left(\frac{\xi^\top(\mu_i-\mu_j)}{2\sigma}\right)^2 = 2\lambda_{ij}(\cos\theta\cos\theta_{ij}+\sin\theta\sin\theta_{ij})^2$$
$$= \lambda_{ij}+\lambda_{ij}\cos(2\theta-2\theta_{ij}) \tag{16}$$

where the parameters λ_{ij} and θ_{ij} are defined as

$$\lambda_{ij}=\frac{\|\mu_i-\mu_j\|^2}{8\sigma^2}, \qquad \theta_{ij}=\operatorname{atan2}\left(\mu_{i,y}-\mu_{j,y},\mu_{i,x}-\mu_{j,x}\right)$$

The rewritten analytical expression highlights the periodicity of the kernel function. Since a pencil of lines is indistinguishable after a rotation of π angle, ARS is π-periodicity $\mathcal{S}_\kappa[f](\theta+\pi)=\mathcal{S}_\kappa[f]$. Hence, the approach based on ARS returns the rotation angle up to angular bias π. The decision on the correct evaluation can be easily solved using simple geometric criteria applied to the result or if there are limits on rotation angle. The exponential of a cosine has an elegant expression into *Fourier series* [53, (9.6.34)]. In particular, the kernel function can be written as

$$\begin{aligned}\psi_{ij}(\theta) &= \exp\left(-\lambda_{ij}+\lambda_{ij}\ \cos(2\theta-2\theta_{ij})\right)\\ &= \exp\left(-\lambda_{ij}\right)\exp\left(\lambda_{ij}\ \cos(2\theta-2\theta_{ij}-\pi)\right)\\ &= \mathrm{e}^{-\lambda_{ij}}\ \left(I_0(\lambda_{ij})+2\sum_{k=1}^{+\infty}I_k(\lambda_{ij})\ \cos(k(2\theta-2\theta_{ij}-\pi))\right)\\ &= a_0^{(ij)}+\sum_{k=1}^{+\infty}\left(a_k^{(ij)}\cos(2k\theta)+b_k^{(ij)}\sin(2k\theta)\right)\end{aligned} \tag{17}$$

where $I_k(\cdot)$ are the modified Bessel functions of the first kind. The coefficients $a_k^{(ij)}$ and $b_k^{(ij)}$ in the above equation are equal to

$$a_k^{(ij)} = 2\ I_k(\lambda_{ij})\ \mathrm{e}^{-\lambda_{ij}}\ (-1)^k\ \cos(2k\theta_{ij}) \tag{18}$$
$$b_k^{(ij)} = 2\ I_k(\lambda_{ij})\ \mathrm{e}^{-\lambda_{ij}}\ (-1)^k\ \sin(2k\theta_{ij}) \tag{19}$$

The above coefficients can be rewritten in a recursive form for $\lambda_{ij} > 0$ and $k \geqslant 2$. This new formula is straightforwardly obtained from the recursive formula of modified Bessel functions $I_k(\lambda_{ij}) = I_{k-2}(\lambda_{ij}) - \frac{2(k-1)}{\lambda_{ij}} I_{k-1}(\lambda_{ij})$. From substitution, we obtain

$$\begin{bmatrix} a_k^{(ij)} \\ b_k^{(ij)} \end{bmatrix} = R(4\theta_{ij}) \begin{bmatrix} a_{k-2}^{(ij)} \\ b_{k-2}^{(ij)} \end{bmatrix} + \frac{2(k-1)}{\lambda_{ij}} R(2\theta_{ij}) \begin{bmatrix} a_{k-1}^{(ij)} \\ b_{k-1}^{(ij)} \end{bmatrix} \tag{20}$$

The series in equation (17) can be arrested to order n (call it $s_n^{(ij)}(\theta)$) and used to compute an approximate value of $\psi_{ij}(\theta)$. The greater is the number n of terms used in the computation the more accurate is the approximation. There are many possible upper bounds for the error achieved by using $s_n(\theta)$. We provide the following one.

Proposition 4. *Let $s_n^{(ij)}(\theta)$ be the Fourier series expansion of eq. (17) arrested to term n-th. Then, if $n > 0$ and $\lambda_{ij} > 0$,*

$$|\psi_{ij}(\theta) - s_n^{(ij)}(\theta)| < \frac{2\mathrm{e}^{-\lambda_{ij}}\ I_n(\lambda_{ij})\ \lambda_{ij}}{n} \tag{21}$$

Proof 4. *The remainder can be bounded as*

$$|\psi_{ij}(\theta) - s_n^{(ij)}(\theta)| \leqslant 2\mathrm{e}^{-\lambda_{ij}} \sum_{k=1}^{\infty} I_{n+k}(\lambda_{ij}) \tag{22}$$

The inequality $(1 + n/\lambda)I_{n+1}(\lambda) < I_n(\lambda)$ holds for any $n > -1$ and $\lambda > 0$ [54]. By recursively applying such inequality, each term of eq. (22) is bound as

$$I_{n+k}(\lambda_{ij}) < I_n(\lambda_{ij}) \prod_{l=1}^{k} \left(\frac{\lambda_{ij}}{\lambda_{ij} + n + l} \right) \leqslant I_n(\lambda_{ij}) \left(\frac{\lambda_{ij}}{\lambda_{ij} + n} \right)^k$$

The above inequality can be substituted into eq. (22) to obtain

$$|\psi_{ij}(\theta) - s_n^{(ij)}(\theta)| < 2\mathrm{e}^{-\lambda_{ij}} I_n(\lambda_{ij}) \sum_{k=1}^{\infty} \left(\frac{\lambda_{ij}}{\lambda_{ij} + n} \right)^k$$

which is a geometric series without the first term and converges to the second member of eq. (21).

Proposition 4 enables to estimate the expansion order required to achieve the desired accuracy. It can be observed that, for large values of λ_{ij}, $I_n(\lambda_{ij}) \simeq e^{\lambda_{ij}}/\sqrt{2\pi\lambda_{ij}}$ [53, (9.7.1)] and, then, the error bound is about $2\sqrt{\lambda_{ij}}/(\sqrt{2\pi}n)$. Thus, the substitution of the expression of λ_{ij} gives us a rule of thumb for approximation error

$$e_n^{(ij)} = \frac{\|\mu_i - \mu_j\|}{2\sqrt{\pi}\ \sigma\ n} \tag{23}$$

The results on the approximation of kernel function can be applied to the GMM-ARS, which has the form of a sum of kernel functions. In particular, the Fourier series expansion of a GMM-ARS is equal to

$$\mathcal{S}_\kappa\left[f\right](\theta) = a_0 + \sum_{k=1}^{+\infty}\left(a_k\cos(2k\theta) + b_k\sin(2k\theta)\right) \tag{24}$$

where the coefficients are

$$a_k = \begin{cases} \frac{1}{\sigma\sqrt{\pi}}\sum_{i=1}^{n_p-1}\sum_{j=i+1}^{n_p} a_0^{(ij)} + \frac{n_p}{2\sigma\sqrt{\pi}} & k = 0 \\ \frac{1}{\sigma\sqrt{\pi}}\sum_{i=1}^{n_p-1}\sum_{j=i+1}^{n_p} a_k^{(ij)} & k > 0 \end{cases} \tag{25}$$

$$b_k = \frac{1}{\sigma\sqrt{\pi}}\sum_{i=1}^{n_p-1}\sum_{j=i+1}^{n_p} b_k^{(ij)} \tag{26}$$

The Fourier series expansion in eq. (24) arrested to the n-th order, $s_n(\theta)$, can be used to approximate the value of the GMM-ARS. The same observations about the approximation $s_n^{(ij)}(\theta)$ hold for the ARS, which consists of several kernel functions $\psi_{ij}(\theta)$. An upper bound of the approximation error of $s_n(\theta)$ is directly derived from Proposition 4.

Corollary 5. *Let $s_n(\theta)$ be the Fourier series expansion of eq. (24) arrested to term n-th. Then,*

$$\left|\mathcal{S}_\kappa\left[f\right](\theta) - s_n(\theta)\right| < \frac{\sum_{i=1}^{n_p-1}\sum_{j=i+1}^{n_p} \mathrm{e}^{-\lambda_{ij}}\ I_n(\lambda_{ij})\ \lambda_{ij}}{n} \tag{27}$$

4.3. Relation to Second Order Moments

PCA-based methods are a standard approach to the estimation of rotation. Such approach exploits the invariance to rotation of the second-order moments

represented by the eigenvalues of the symmetric cross-covariance matrix. The rotation angle between two point sets is computed by comparing the directions of the principal axes (aka eigenvectors) of the respective cross-covariance matrices. The ARS is related to the second-order moments of a point set. Following the notation of section 4.1, let $d_{ij} = (\mu_i - \mu_j)/2\sigma$ be the normalized pairwise positions of points i-th and j-th, $\bar{\mu} = \frac{1}{n_p}\sum_{i=1}^{n_p}\mu_i$ be the centroid (first-order moment) of the point set, and $d_i = (\mu_i - \bar{\mu})/2\sigma$ be the positions to centroid of point $i-th$. Two results enable the computation of a lower bound for the ARS.

1. ARS kernels are inferiorly bound by

$$\psi_{ij}(\theta) = \exp\left(-(\xi^\top d_{ij})^2\right) \geq 1 - \xi^\top d_{ij} d_{ij}^\top \xi \tag{28}$$

2. The cross-covariance matrix can be rewritten w.r.t. the sum of all pairwise positions as

$$\bar{\Sigma} = \frac{1}{n_p}\sum_{i=1}^{n_p} d_i d_i^\top = \frac{1}{n_p^2}\sum_{i=1}^{n_p-1}\sum_{j=i+1}^{n_p} d_{ij} d_{ij}^\top \tag{29}$$

Using equations (28) and (29) in equation (12), the ARS has a lower bound with the following expression:

$$\begin{aligned}\mathcal{S}_\kappa[f](\theta) &\geq \frac{n_p}{2\sigma\sqrt{\pi}} + \frac{1}{\sigma\sqrt{\pi}}\sum_{i=1}^{n_p-1}\sum_{j=i+1}^{n_p}\left(1 - \xi^\top d_{ij} d_{ij}^\top \xi\right) \\ &= \frac{n_p^2}{2\sigma\sqrt{\pi}} - \frac{n_p^2}{\sigma\sqrt{\pi}}\xi^\top \bar{\Sigma}\xi = \Lambda(\theta)\end{aligned} \tag{30}$$

The quadratic function $\Lambda(\theta)$ in eq. (30) is maximum when ξ is the eigenvector corresponding to the minimum eigenvalue of the cross-covariance matrix $\bar{\Sigma}$. Indeed, PCA-based methods estimate the rotation by aligning the eigenvectors of the corresponding cross-covariance matrices. If the ratio between the maximum and minimum eigenvalues of $\bar{\Sigma}$ is large, i.e. there is a strong central direction for points, then $\Lambda(\theta)$ accurately approximates the ARS. In general, $\Lambda(\theta)$ is more sensitive to the distribution of points than ARS and its trend may not provide sufficient characterisation of dominant directions.

5. Estimation of Rotation

5.1. Correlation of the ARS

The GMM-ARS presented in the previous section is an effective tool for measuring the importance of a specific orientation θ in a point set. An important property of this function is the translation invariance and rotational shift stated in Proposition 3. Like the Hough Spectrum [29], such property can be exploited to compare and estimate the rotation between two point sets. If two point sets represent the same scene observed from different viewpoints, then the transformation that aligns the two sets is estimated as the joint composition of rotation and translation. However, since their GMM-ARS is independent from translation, the evaluation of rotation is decoupled from the evaluation of translation.

Let $f_S(r)$ and $f_T(r)$ be respectively the density functions of the source and the target point sets, $\mathcal{S}_\kappa\left[f_S\right](\theta)$ and $\mathcal{S}_\kappa\left[f_T\right](\theta)$ be the respective GMM-ARS. Suppose that $f_T(r)$ represents the rotated version of $f_S(r)$, except from noise and field-of-view issues commonly occurring in perception problems. The rotation between $f_S(r)$ and $f_T(r)$ can be found by searching the angular shift δ that maximizes the overlap between the two spectra. The overlap is measured by the function

$$C(\delta) = \frac{1}{\pi}\int_0^\pi \mathcal{S}_\kappa\left[f_S\right](\theta+\delta)\ \mathcal{S}_\kappa\left[f_T\right](\theta)\ d\theta \tag{31}$$

which represents the correlation of the two spectra. The correlation $C(\theta)$ can be written as a sum of modified Bessel functions. This follows by the observation that the product of $\mathcal{S}_\kappa\left[f_S\right](\theta)$ and $\mathcal{S}_\kappa\left[f_T\right](\theta)$ consists of products of kernel functions. If $\psi^S(\theta)$ and $\psi^T(\theta)$ are kernels of respectively the reference and transformed spectra, then

$$\begin{aligned}
&\frac{1}{\pi}\int_0^\pi \psi^S(\theta+\delta)\psi^T(\theta)d\theta = \\
&\quad = \frac{1}{\pi}\int_0^\pi \exp\left(-K_{RT} - M_{RT}\cos(2\theta-\phi_{RT})\right)d\theta \\
&\quad = \mathrm{e}^{-K_{RT}}\ I_0(M_{RT})
\end{aligned} \tag{32}$$

where, given λ_S and λ_T defined as in eq. (16),

$$\begin{aligned} M_{ST}\ \cos\phi_{ST} &= \lambda_S \cos(2\theta_S + 2\delta) + \lambda_T \cos(2\theta_T) \\ M_{ST}\ \sin\phi_{ST} &= \lambda_S \sin(2\theta_S + 2\delta) + \lambda_T \sin(2\theta_T) \\ K_{ST} &= \lambda_S + \lambda_T \end{aligned}$$

The correlation function is the sum of terms in eq. (32). Unfortunately, the analytical expression is difficult to use in practice. If both the source and the target point sets consist of n_p points, then the evaluation of $C(\delta)$ has computational complexity $O(n_p^4)$, since $\mathcal{S}_\kappa[f_S](\theta)$ and $\mathcal{S}_\kappa[f_T](\theta)$ have each $O(n_p^2)$ terms. Moreover, the manipulation of eq. (32) and of the derived terms, e.g. to search maxima of correlation, is rather difficult and not practical.

The Fourier series expansion of GMM-ARS provides a viable approach to the efficient evaluation of $C(\delta)$. Equation (31) is very close to the convolution of two GMM-RSs. There is a well-known result about Fourier series of convolution that can be exploited.

Proposition 6. *Let $\mathcal{S}_\kappa[f_S](\theta)$ and $\mathcal{S}_\kappa[f_T](\theta)$ be the GMM-RSs of respectively the reference and the transformed point sets. Let $\{a_k^S, b_k^S\}_k$ and $\{a_k^T, b_k^T\}_k$ be the respective Fourier series coefficients. Then,*

$$C(\delta) = a_0^C + \sum_{k=1}^{+\infty} \left(a_k^C \cos(2k\delta) + b_k^C \sin(2k\delta)\right) \tag{33}$$

where $a_k^C = \frac{a_k^T a_k^R + b_k^T b_k^R}{2}$ and $b_k^C = \frac{a_k^T b_k^R - b_k^T a_k^R}{2}$.

Proof 5. *Let the terms of Fourier series of reference and transformed spectra be respectively*

$$\begin{aligned} \omega_k^S(\theta) &= a_k^S \cos(2k(\theta+\delta)) + b_k^S \sin(2k(\theta+\delta)) \\ \omega_i^T(\theta) &= a_i^T \cos(2i\theta) + b_i^T \sin(2i\theta) \end{aligned}$$

$C(\delta)$ is the sum of the integrals of $\omega_k^S(\theta)\omega_i^T(\theta)$ over $\theta \in [0, \theta[$. If $i \neq k$, then such integral is equal to 0. Given $i = k$, $\omega_k^S(\theta)\omega_i^T(\theta)$ can be expanded using Werner formulas and integrated. The only non-zero terms are linear combination of $\cos(2k\delta)$ and $\sin(2k\delta)$, which are collected as in eq. (33).

5.2. Computation of the ARS Correlation Maximum

In section 5.1, the rotation angle corresponds to the global maximum of the ARS correlation function. Among the potential approaches, branch and bound techniques [55] provide a robust and easy-to-implement solution for this problem. A branch and bound algorithm recursively divides the objective function domain into subintervals and provides the upper and lower bound values for the function over each subinterval. The correlation function $C(\theta)$ has been expressed through its Fourier serie expansion in eq. (33), a general form suitable for interval arithmetic. The interval arithmetic of sine and cosine functions is well defined: given an interval $\mathcal{X} = [\theta_0, \theta_1]$, the lower and upper bounds of $\cos\theta$ (and similarly of $\sin\theta$) for $\theta \in \mathcal{X}$, are computed by checking whether critical points $(\frac{1}{2} + i)\pi$ with $i \in \mathbb{Z}$ are contained in $\mathcal{X}$. Let $\underline{g_k}$ and $\overline{g_k}$ be respectively the lower and upper bounds of the sinusoid $g_k(\theta) = a_k \cos(2k\delta) + b_k \sin(2k\delta)$ on interval $\mathcal{X}$. Thus, the upper and lower bounds of the Fourier series $F(\theta)$ are obtained by summing the contributions of all its terms g_k with $k = 0, \ldots, n$ according to interval arithmetic sense. In particular, the values of $F(\theta)$ over $\mathcal{X}$ are contained in interval $[\sum_{k=0}^{n} \underline{g_k}, \sum_{k=0}^{n} \overline{g_k}]$.

The same procedure can be used for searching the global maximum of both the ARS and ARS correlation. In summary, the procedure for rotation estimation consists of the following steps.

1. Given the source and target point sets, respectively $\mathcal{P}_S$ and $\mathcal{P}_T$, compute the corresponding ARS $\mathcal{S}_\kappa[f_S](\theta)$ and $\mathcal{S}_\kappa[f_T](\theta)$ in the form of Fourier series as in eq. (24).
2. Compute the correlation $C(\delta)$ of the spectra $\mathcal{S}_\kappa[f_S](\theta)$ and $\mathcal{S}_\kappa[f_T]$, also in the form of Fourier series, according to eq. (33).
3. Push the initial domain interval $\mathcal{X} = [0, \pi]$ and the corresponding interval bounds of $C(\delta)$, $\mathcal{Y} = [\underline{C}, \overline{C}]$, into queue $\mathcal{Q}$. Initialize the estimate of maximum interval $(\mathcal{X}_{max}, \mathcal{Y}_{max}) \leftarrow (\mathcal{X}, \mathcal{Y})$.
4. Pop from queue $\mathcal{Q}$ the pair $(\mathcal{X} = [\underline{x}, \overline{x}], \mathcal{Y} = [\underline{y}, \overline{y}])$ with maximum $\overline{y}$.
5. If $\overline{y} < \underline{y_{max}}$, then ignore the current interval and return to 4.

6. If $\underline{y} > \overline{y_{max}}$, then update the estimate of maximum interval $(\mathcal{X}_{max}, \mathcal{Y}_{max}) \leftarrow (\mathcal{X}, \mathcal{Y})$.
7. If the domain interval dimension is greater than tolerance, i.e. $|\overline{x} - \underline{x}| > \epsilon_\theta$, then
   - split $\mathcal{X}$ into two domain intervals $\mathcal{X}^L$ and $\mathcal{X}^H$;
   - compute the bounds $\mathcal{Y}^L$ and $\mathcal{Y}^H$ of correlation function $C(\delta)$ over respectively $\mathcal{X}^L$ and $\mathcal{X}^H$;
   - push $(\mathcal{X}^L, \mathcal{Y}^L)$ and $(\mathcal{X}^H, \mathcal{Y}^H)$ into queue $\mathcal{Q}$.
8. Repeat from 4 until there are items in $\mathcal{Q}$. Otherwise, return the estimate of maximum point and value $(\mathcal{X}_{max}, \mathcal{Y}_{max})$.

The accuracy in correlation maximum estimation depends on optimization tolerance ϵ_θ as discussed in experiments.

6. Experiments

The experiments presented in this section have been designed to assess the accuracy of the proposed method in estimating the rotation. The compared methods for rotation estimation include the ARS, the HS, the PCA, the ICP, and the VFC. Except when explicitly declared, the proposed method ARS is applied with fixed values of standard deviation $\sigma = 2$, Fourier expansion order $n = 20$ and optimization tolerance $\epsilon_\theta = 0.5\ deg$. Hence, the rotation estimation does not exploit any information about the noise level applied in the experiments illustrated in the following. The dimension of Hough transform cells is $\Delta\theta = 0.5°$ and $\Delta\rho = 2$. PCA algorithm computes rotation angle by aligning the principal axes of the point set, i.e. the eigenvectors of its covariance matrix. PCA is also used as initial guess for the correspondence based methods that cannot operate if not close to the target point set. In particular, the angle is estimated by aligning the principal axes of the covariance matrix and the translation is given by the centroid displacement. The implementation of ICP used in the experiments

searches correspondences according to standard nearest neighbor policy[2]. The nearest neighbor policy is also used to compute the putative correspondences that are refined by the VFC [13]. As discussed in section 2, VFC removes outliers and keeps only the matches that can be overlapped by a unique consistent rigid transformation.

A preliminary set of experiments have been performed to assess the impact of resolution parameters on rotation estimation methods HS and ARS. The accuracy of HS depends on the resolution $\Delta\theta$ of its histogram bins, since rotation angle is estimated by finding the maximum of histogram correlation. In the case of ARS, the evaluation of rotation is affected by the tolerance ϵ_θ that stops the branch-and-bound optimization described in section 5.2. The value of Gaussian kernel standard deviation σ_i and the Fourier series order n have more limited impact on the final result. Experiments have been performed on a subset of 61 shapes from MPEG-7 dataset belonging to different object categories discussed later in this section. No transformation has been applied to the points representing each shape. Figure 3 shows the mean error obtained by HS and ARS. It is apparent that the ARS achieves better accuracy than HS except when the HS resolution is pretty small, i.e. less than 0.1 *deg*. It would be wrong to infer from this experiment on a dataset without transformation that the lowest values of $\Delta\theta$ and ϵ_θ achieves the best results. Smaller values of angular resolution makes estimation less robust to noise.

The point sets used in our experiments are taken from the MPEG-7 shape database [56]. The points of each set correspond to the contour pixels of the original input images. The dataset consists of 1400 images belonging to 70 different shape categories (e.g. dog, bottle, guitar, tree). Although the dataset is designed to perform comparisons among the items belonging to a category, our experiments compare rotated, translated and transformed copies derived from the same original item. This procedure gives complete control on the value of rotation angle and performs comparisons between different views of the same

[2]http://www.cvlibs.net/.

object. Besides aligning pairs of rotated and translated copies of a given point set, three different transformations have been applied to assess the robustness of the rotation estimation.

1. *Noise.* This transformation adds Gaussian noise with a given standard deviation σ to the coordinates of the points. The value of σ is varied in interval $0 \div 50$, where the maximum dimension of a point set may varies from 300 to 900.
2. *Occlusion.* An occluded version of a point set is generated by randomly generating a circle and removing all the points lying inside this circle. The center of the circle is a randomly chosen point of the dataset and the radius is proportional to the size of the point set. In particular, if the points are contained in a bounding box of size $b_x \times b_y$, the radius is equal to $\beta\sqrt{b_x b_y}$, where $0 \leqslant \beta \leqslant 1$ is the occlusion rate. Occlusion rate β is varied up to 50%.
3. *Random Points.* This transformation adds $\gamma\ n_{in}$ random points to an input point set of n_{in} points, where γ is the random point rate. The random points are uniformly distributed on a circle centered on the point set mean point and with radius doubling the size of bounding box. The maximum value of random point rate γ used in the tests is 300%, i.e. the random points are at most 3 times the number of shape points.

A transformed dataset is obtained by generating two rotated and translated copies of each of the 1400 shapes. The rotation angles are uniformly distributed on interval $[0, 180]$ *deg*, whereas the translation is uniformly distributed up to a maximum value approximately corresponding to the dimension of the object. The desired transformation (random noise, occlusion and additional random points) is independently applied to each of the point sets. The point set pairs are the inputs of the compared rotation estimation algorithms. Since the rotation is randomly generated, the groundtruth is available to assess their performance. Figure 4 shows several examples of point sets obtained by applying the random transformations. Each subfigure contains the source shape (Src) to be rotated

with destination shape (Dst) within the source shape rotated according to the estimation of ARS, HS and VFC. In most cases, it is difficult to qualitatively appreciate the differences in rotation estimation, except for example *hammer-11* showing a successful outcome of ARS and a failure of both HS and VFC. The legend reports the correct rotation angle (Dst) and the values computed with ARS, HS and VFC in order to give more insight to the reader.

Figures 5, 6 and 7 respectively illustrate the outcomes of noise, occlusion and random point tests. Each figure shows the positive estimation rate on the top subfigure and the mean angular error on the bottom one both w.r.t. the transformation parameter. For each test, the positive rotation estimations are those achieving an angular error less than 5°. The mean angular error has been computed only for positive rotation estimations to avoid the influence of wrong estimations. ARS and HS have similar performance in all the three tests as it was expected due to the strong relationship between Radon and Hough transforms [37]. When no noise or occlusion is applied, the angular error is less than 0.5° for both. VFC performs better than all the other techniques in noise test (Figure 5) both in positive estimation and angular error. In this case, there is a correct match for all points and, in spite of noise, VFC effectively filters the outliers in putative correspondences. However, its performance significantly drops in occlusion and random point tests. In these experiments, there are points without a correspondence in the other point sets due to occlusion or there are two many potential match due to the augmented number of points. The non-matching points and the high number of outliers strongly affect the outcome of robust correspondence algorithms like VFC. In general, these experiments show that rotation estimation is more sensitive to occlusion, whereas ARS and HS are robust to noise. ARS achieves larger positive rates and smaller angular error than HS in noise test, whereas HS has slightly better performance in occlusion and and random points tests. Both ARS and HS outperform PCA and ICP, which are more sensitive to differences between the point sets to be aligned. Also VFC achieves better results than PCA and ICP being sort of their refinement.

A separate analysis has been performed on each of the 70 shape categories

of MPEG-7 dataset. Tables 1, 2 and 3 respectively illustrate the outcomes of noise, occlusion and random point tests divided according to shape category. The histograms of noise test are obtained with $\sigma = 20.0$, those of occlusion with rate $\beta = 20\%$ and those of additive randon points to rate $\gamma = 100\%$. The less robust techniques like PCA and ICP achieves positive rates and mean errors similar to ARS and HS only in the case of elongated objects with strong principal direction like *Bone*, *bat*, *elephant*, *deer* subject to Gaussian noise. However, occlusion and to less extent random points affect rotation estimation of PCA, ICP and VFC also with these shapes. The mean error on rotation angle of ARS and HS is larger for shapes with central symmetries or with a limited number of aligned points, like *apple*, *bell*, *chopper*, *cup* and *face*.

Table 4 illustrates the average execution times of the algorithms used in the experiments. The experiments have been performed using a Intel i7-3630QM CPU @ 2.40GHz, 8 GB RAM. The execution time of ARS is ostensibly the larger of all the compared algorithms due to the quadratic complexity of ARS with respect to the number of points as observed in Section 4.1. Despite this drawback, consistent improvements in its execution time may be achieved by more careful and parallel implementations, and especially by more efficient representation of the input point sets with GMMs. While the current policy associate a Gaussian kernel to each point, each kernel could summarize a point subset with central distribution.

7. Conclusion

In this paper, we have proposed a novel method for global rotation estimation between planar point sets. The translation and angular-shift invariance of the ARS enables the decoupling of rotation and translation. Rotation angle is computed by searching the global maximum of a correlation function. The ARS has been formally defined from the RT of a GMM consisting of isotropic and identical kernels. Moreover, we have proposed an efficient approximation of the spectrum and its correlation through its exact Fourier expansion. The

proposed method has been implemented and compared with other state-of-the-art algorithms. The experiments demonstrated the accuracy of the proposed method and its robustness to noise, occlusion and random points. ARS outperforms correspondence-based methods including one state-of-the-art algorithm and achieves similar results to HS. In future works, we expect to extend Radon Spectrum to the case of non-isotropic kernel and to improve its computational performance.

Acknowledgements

The author would like to thank professor Stefano Caselli, for several fruitful discussions about experimental assessment of the proposed method.

References

[1] S. Carpin, Merging maps via Hough Transform, in: Proc. of the IEEE/RSJ Int. Conf. on Intelligent Robots and Systems (IROS), 2008, pp. 1878–1883.

[2] D. Lodi Rizzini, S. Caselli, Metric-topological maps from laser scans adjusted with incremental tree network optimizer, Robotics & Autonomous Systems 57 (10) (2009) 1036 – 1041. doi:10.1016/j.robot.2009.07.022.

[3] A. Mandow, J. Martnez, A. Reina, J. Morales, Fast range-independent spherical subsampling of 3d laser scanner points and data reduction performance evaluation for scene registration, Pattern Recognition Letters 31 (11) (2010) 1239 – 1250. doi:10.1016/j.patrec.2010.03.008.

[4] L. Latecki, R. Lakaemper, Convexity Rule for Shape Decomposition Based on Discrete Contour Evolution, Computer Vision and Image Understanding 73 (3) (1999) 441–454. doi:10.1006/cviu.1998.0738.

[5] L. Latecki, R. Lakamper, Shape similarity measure based on correspondence of visual parts, IEEE Trans. on Pattern Analysis and Machine Intelligence 22 (10) (2000) 1185–1190. doi:10.1109/34.879802.

[6] M. Grogan, R. Dahyot, Shape registration with directional data, Pattern Recognition 79 (2018) 452–466. doi:10.1016/j.patcog.2018.02.021.

[7] R. So, A. Chung, A novel learning-based dissimilarity metric for rigid and non-rigid medical image registration by using Bhattacharyya Distances, Pattern Recognition 62 (2017) 161–174. doi:10.1016/j.patcog.2016.09.004.

[8] P. Besl, H. Mckay, A method for registration of 3-d shapes, IEEE Trans. Pat. Anal. Mach. Intel 14 (2) (1992) 239–256.

[9] P. Biber, W. Straßer, The normal distributions transform: A new approach to laser scan matching, in: Proc. of the IEEE/RSJ Int. Conf. on Intelligent Robots and Systems (IROS), 2003, pp. 2743–2748.

[10] Y. Liu, Improving icp with easy implementation for free-form surface matching, Pattern Recognition 37 (2) (2004) 211–226. doi:10.1016/S0031-3203(03)00239-5.

[11] M. Magnusson, A. Lilienthal, T. Duckett, Scan registration for autonomous mining vehicles using 3d-ndt, Journal of Field Robotics 24 (10) (2007) 803–827.

[12] S. Du, N. Zheng, S. Ying, J. Liu, Affine iterative closest point algorithm for point set registration, Pattern Recognition Letters 31 (9) (2010) 791–799. doi:10.1016/j.patrec.2010.01.020.

[13] J. Ma, J. Zhao, J. Tian, A. Yuille, Z. Tu, Robust Point Matching via Vector Field Consensus, IEEE Transactions on Image Processing 23 (4) (2014) 1706–1721. doi:10.1109/TIP.2014.2307478.

[14] D. Holz, A. Ichim, F. Tombari, R. Rusu, S. Behnke, Registration with the point cloud library: A modular framework for aligning in 3-d, IEEE Robotics Automation Magazine 22 (4) (2015) 110–124. doi:10.1109/MRA.2015.2432331.

[15] J. Ma, W. Qiu, J. Zhao, Y. Ma, A. Yuille, Z. Tu, Robust l_2e estimation of transformation for non-rigid registration, IEEE Transactions on Signal Processing 63 (5) (2015) 1115–1129. doi:10.1109/TSP.2014.2388434.

[16] J. Ma, J. Zhao, A. Yuille, Non-rigid point set registration by preserving global and local structures, IEEE Transactions on Image Processing 25 (1) (2016) 53–64.

[17] A. Myronenko, X. Song, Point set registration: Coherent point drift, IEEE Trans. on Pattern Analysis and Machine Intelligence 32 (12) (2010) 2262–2275. doi:10.1109/TPAMI.2010.46.

[18] J. Ma, J. Zhao, A. Yuille, Non-rigid point set registration by preserving global and local structures, IEEE Transactions on Image Processing 25 (1) (2016) 53–64. doi:10.1109/TIP.2015.2467217.

[19] C. Brechbuhler, G. Gerig, O. Kubler, Parametrization of closed surfaces for 3-d shape description, Computer Vision and Image Understanding 61 (2) (1995) 154–170.

[20] A. Makadia, A. Patterson, K. Daniilidis, Fully automatic registration of 3d point clouds, in: Proc. of IEEE Computer Vision and Pattern Recognition (CVPR), Vol. 1, 2006, pp. 1297–1304.

[21] A. Makadia, K. Daniilidis, Rotation recovery from spherical images without correspondences, IEEE Trans. on Pattern Analysis and Machine Intelligence 28 (7) (2006) 1170–1175.

[22] M. Kazhdan, An approximate and efficient method for optimal rotation alignment of 3D models, IEEE Trans. on Pattern Analysis and Machine Intelligence 29 (7) (2007) 1221–1229.

[23] S. Althloothi, M. Mahoor, R. Voyles, A robust method for rotation estimation using spherical harmonics representation, IEEE Trans. on Image Processing 22 (6) (2013) 2306–2316.

[24] B. Zitova, J. Flusser, Image registration methods: a survey, Image and vision computing 21 (11) (2003) 977–1000.

[25] G. Evangelidis, E. Psarakis, Parametric image alignment using enhanced correlation coefficient maximization, IEEE Trans. on Pattern Analysis and Machine Intelligence 30 (10) (2008) 1858–1865.

[26] J. Ho, M. Yang, On affine registration of planar point sets using complex numbers, Computer Vision and Image Understanding 115 (1) (2011) 50–58.

[27] J. Lezama, J. Morel, G. Randall, R. Gioi, A contrario 2d point alignment detection, IEEE Trans. on Pattern Analysis and Machine Intelligence 37 (3) (2015) 499–512. doi:10.1109/TPAMI.2014.2345389.

[28] Y. Kim, S. Kim, Collinear groupwise feature selection via discrete fusion group regression, Pattern Recognition 83 (2018) 1 – 13. doi:10.1016/j.patcog.2018.05.013.

[29] A. Censi, L. Iocchi, G. Grisetti, Scan Matching in the Hough Domain, in: Proc. of the IEEE Int. Conf. on Robotics & Automation (ICRA), 2005, pp. 2739–2744. doi:10.1109/ROBOT.2005.1570528.

[30] A. Censi, S. Carpin, HSM3D: feature-less global 6DOF scan-matching in the Hough/Radon domain, in: Proc. of the IEEE Int. Conf. on Robotics & Automation (ICRA), 2009, pp. 3899–3906.

[31] R. Duda, P. Hart, Use of the hough transformation to detect lines and curves in pictures, Commun. ACM 15 (1) (1972) 11–15. doi:10.1145/361237.361242.

[32] M. A. Carreira-Perpinan, Mode-finding for mixtures of Gaussian distributions, IEEE Trans. on Pattern Analysis and Machine Intelligence 22 (11) (2000) 1318–1323.

[33] H. Edelsbrunner, B. Fasy, G. Rote, Add isotropic gaussian kernels at own risk: More and more resilient modes in higher dimensions, in: Proc. of

the 28th Annual Symposium on Computational Geometry (SOCG), ACM, 2012, pp. 91–100.

[34] J. Fan, J. Yang, D. Ai, L. Xia, Y. Zhao, X. Gao, Y. Wang, Convex hull indexed Gaussian mixture model (CH-GMM) for 3D point set registration, Pattern Recognition 59 (2016) 126–141. doi:10.1016/j.patcog.2016.02.023.

[35] S. Deans, Radon and Abel Transforms, in: A. Poularikas (Ed.), The Transforms and Applications Handbook, 2nd Edition, CRC Press, 2000, pp. 1–95.

[36] N. Nacereddine, S. Tabbone, D. Ziou, Similarity transformation parameters recovery based on radon transform. application in image registration and object recognition, Pattern Recognition 48 (7) (2015) 2227–2240. doi:10.1016/j.patcog.2015.01.017.

[37] M. van Ginkel, C. Luengo Hendriks, L. van Vliet, A short introduction to the Radon and Hough transforms and how they relate to each other, Tech. Rep. Number QI-2004-01, Quantitative Imaging Group, Imaging Science & Technology Department, TU Delft (2004).

[38] S. Gold, A. Rangarajan, C.-P. Lu, S. Pappu, E. Mjolsness, New algorithms for 2D and 3D point matching: Pose estimation and correspondence, Pattern recognition 31 (8) (1998) 1019–1031.

[39] B. Horn, Closed-form solution of absolute orientation using unit quaternions, J. Opt. Soc. Amer. 4 (4) (1987) 629–642.

[40] R. Toldo, A. Beinat, F. Crosilla, Global registration of multiple point clouds embedding the Generalized Procrustes Analysis into an ICP framework, in: 5th Int. Symposium 3D Data Processing, Visualization and Transmission (3DPVT2010), 2010, pp. 1–6.

[41] J. Aleotti, D. Lodi Rizzini, R. Monica, S. Caselli, Global Registration of Mid-Range 3D Observations and Short Range Next Best Views, in: Proc. of

the IEEE/RSJ Int. Conf. on Intelligent Robots and Systems (IROS), 2014, pp. 3668–3675. doi:10.1109/IROS.2014.6943077.

[42] Y. Yang, S. Ong, K. Foong, A robust global and local mixture distance based non-rigid point set registration, Pattern Recognition 48 (1) (2015) 156–173. doi:10.1016/j.patcog.2014.06.017.

[43] M. Fischler, R. Bolles, Random Sample Consensus: A Paradigm for Model Fitting with Applications to Image Analysis and Automated Cartography, Commun. ACM 24 (6) (1981) 381–395. doi:10.1145/358669.358692.

[44] P. Torr, A. Zisserman, MLESAC: A New Robust Estimator with Application to Estimating Image Geometry, Computer Vision and Image Understanding 78 (1) (2000) 138–156.

[45] J. Tangelder, R. Veltkamp, A survey of content based 3d shape retrieval methods, Multimedia Tools and Applications 39 (3) (2008) 441–471. doi:10.1007/s11042-007-0181-0.

[46] R. Hoover, A. Maciejewski, R. Roberts, Eigendecomposition of images correlated on, and using spectral theory, Image Processing, IEEE Transactions on 18 (11) (2009) 2562–2571.

[47] E. De Castro, C. Morandi, Registration of translated and rotated images using finite fourier transforms, IEEE Trans. on Pattern Analysis and Machine Intelligence (5) (1987) 700–703.

[48] B. Reddy, B. Chatterji, An fft-based technique for translation, rotation, and scale-invariant image registration, IEEE Trans. on Image Processing 5 (8) (1996) 1266–1271.

[49] S. Zokai, G. Wolberg, Image registration using log-polar mappings for recovery of large-scale similarity and projective transformations, IEEE Trans. on Image Processing 14 (10) (2005) 1422–1434. doi:10.1109/TIP.2005.854501.

[50] F. Kallasi, D. Lodi Rizzini, S. Caselli, Fast keypoint features from laser scanner for robot localization and mapping, RAL 1 (1) (2016) 176–183, dOI 10.1109/LRA.2016.2517210. doi:10.1109/LRA.2016.2517210.

[51] J. Illingworth, J. Kittler, A survey of the hough transform, Computer Vision, Graphics, and Image Processing 44 (1) (1988) 87–116. doi:10.1016/S0734-189X(88)80033-1.

[52] K. Petersen, M. Pedersen, The Matrix Cookbook, version 20121115 (Nov 2012).
URL http://www2.imm.dtu.dk/pubdb/p.php?3274

[53] M. Abramowitz, I. Stegun, Handbook of Mathematical Functions, Dover Publications, 1965.

[54] C. Joshi, S. Bissu, Some inequalities of Bessel and modified Bessel functions, J. Australian Mathematical Society (Series A) 50 (1991) 333–342. doi:10.1017/S1446788700032791.

[55] M. Locatelli, F. Schoen, Global optimization: theory, algorithms, and applications, SIAM, 2013.

[56] X. Bai, X. Yang, L. Latecki, W. Liu, Z. Tu, Learning context-sensitive shape similarity by graph transduction, IEEE Trans. on Pattern Analysis and Machine Intelligence 32 (5) (2010) 861–874. doi:10.1109/TPAMI.2009.85.

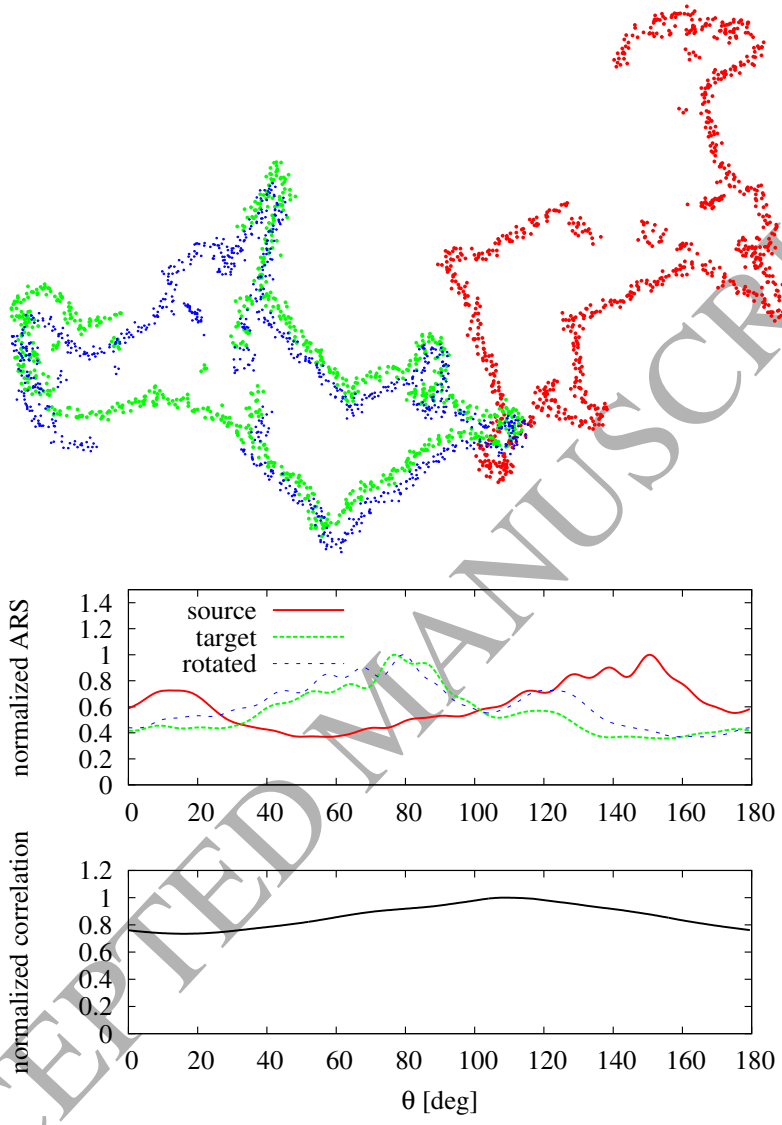

Figure 1: Example of rotation estimation with ARS. Top: source (red) and target (green) point sets with the source set rotated according to ARS estimation and approximately translated according to centroid displacement (blue). The source and target sets are generated from the same point set by applying additive noise with standard deviation $\sigma_n = 2$ and occlusion with $\beta = 20\%$ rate (defined in Section 6). Bottom: normalized ARS of source (red), target (green) and rotated source (blue) point sets with the correlation function (black) of the two original sets.

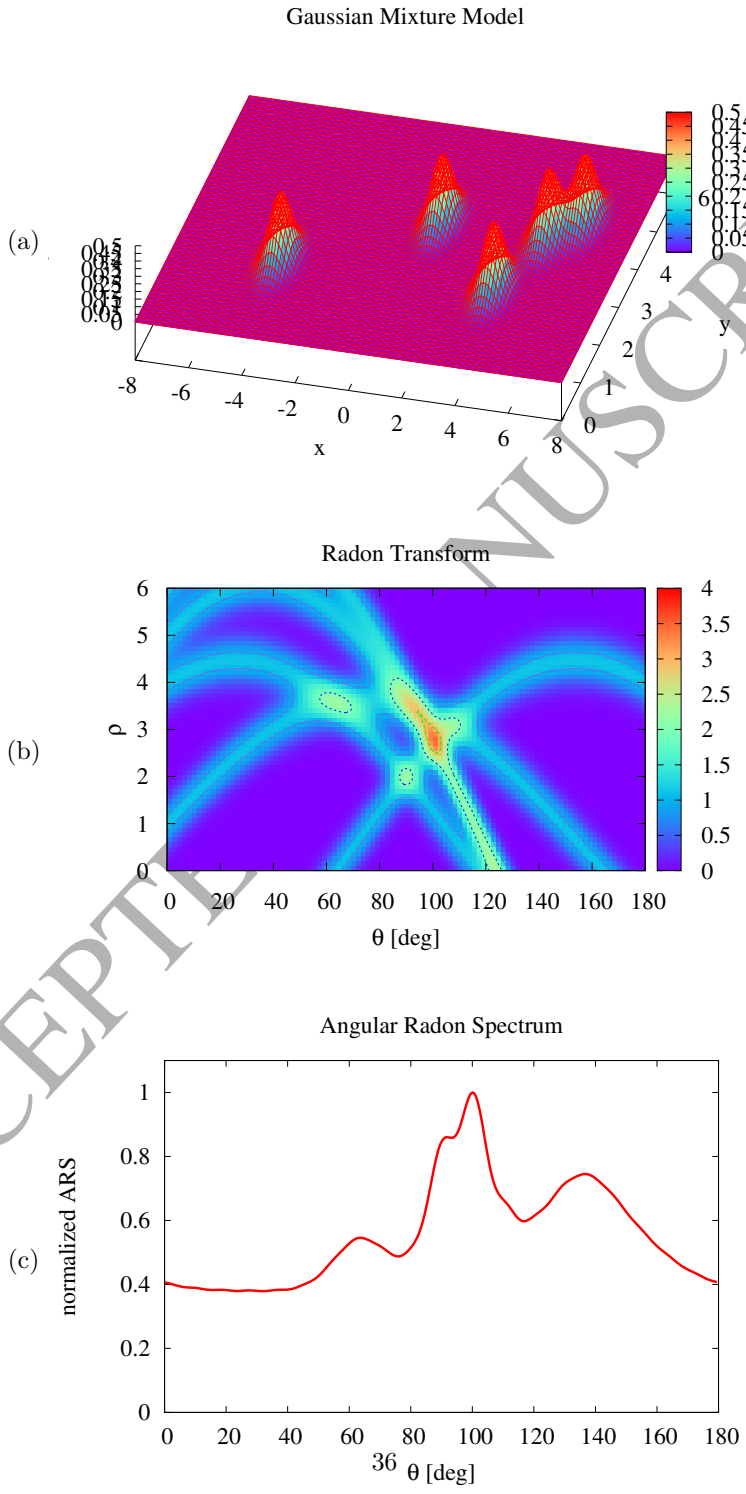

Figure 2: An example of a GMM consisting of 5 identical and isotropic kernels with $\sigma = 0.35$ (a), the corresponding RT (b) and ARS (c).

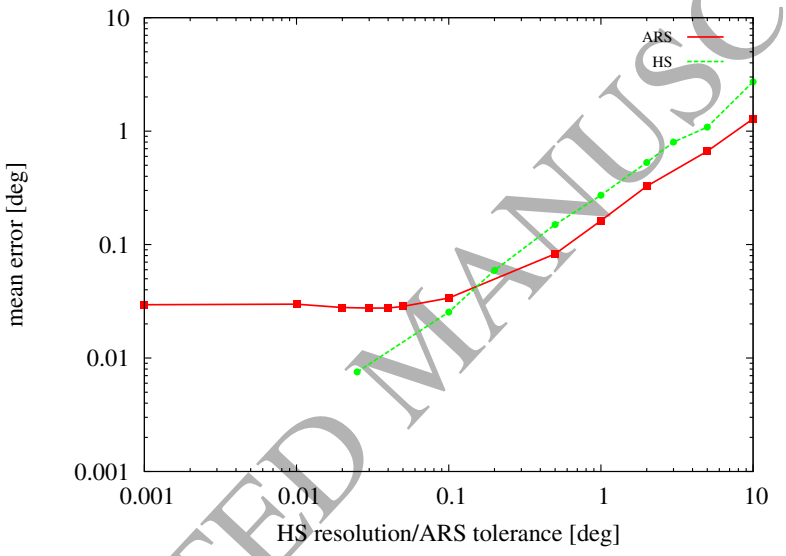

Figure 3: Rotation angle mean error of ARS and HS achieved with different values of ARS optimization tolerance ϵ_θ or of HS bin resolution $\Delta\theta$. The experiment is performed on a dataset of 61 shapes belonging to different shape categories and without applying transformations.

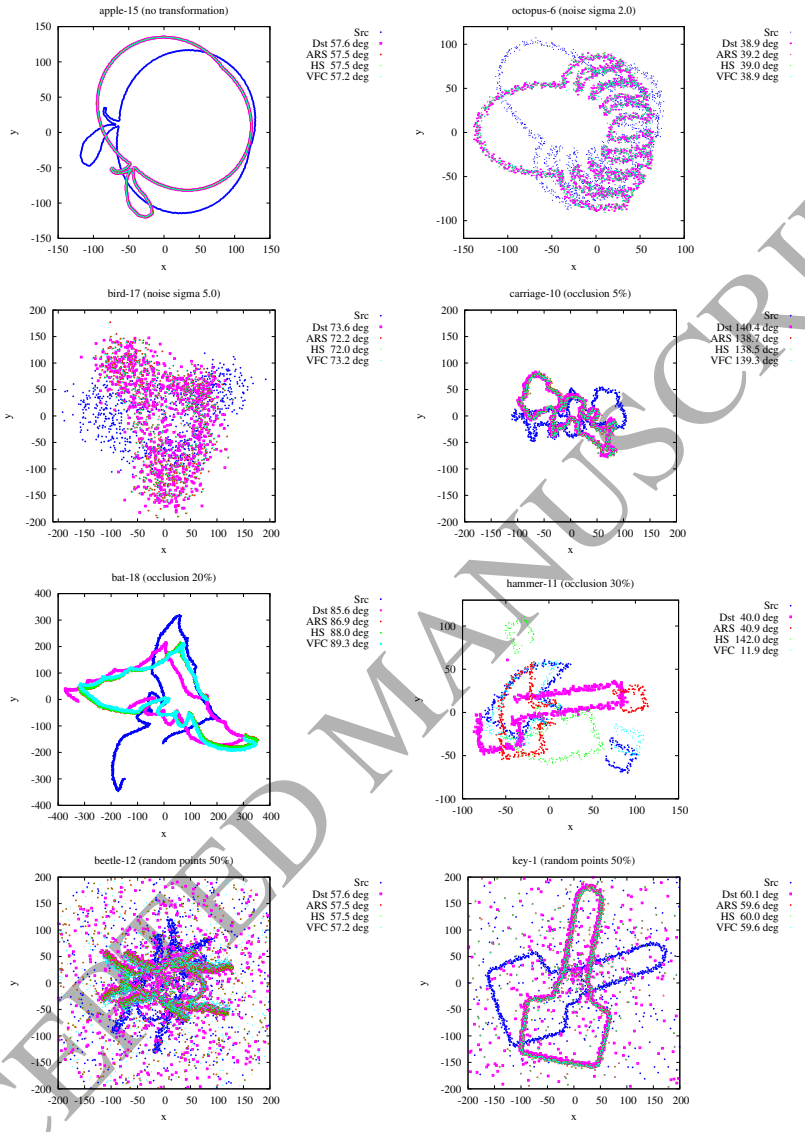

Figure 4: Examples of shape registration: *apple-15* (no transformation); *octopus-6* and *bird-17* (noise tests); *carriage-10*, *bat-18* and *hammer-11* (occlusion from 5% to 30%); *beetle-12* and *key-1* (random points 50%). The source shape (Src) is rotated in order to overlap with destination shape (Dst) using ARS, HS and VFC to estimate rotation angle. The correct and estimated values of rotation are displayed in the legend alongside with Dst, ARS, HS and VFC. Since the translation is not estimated, the shapes are centered on their centroids (which may not overlap, especially with occlusion).

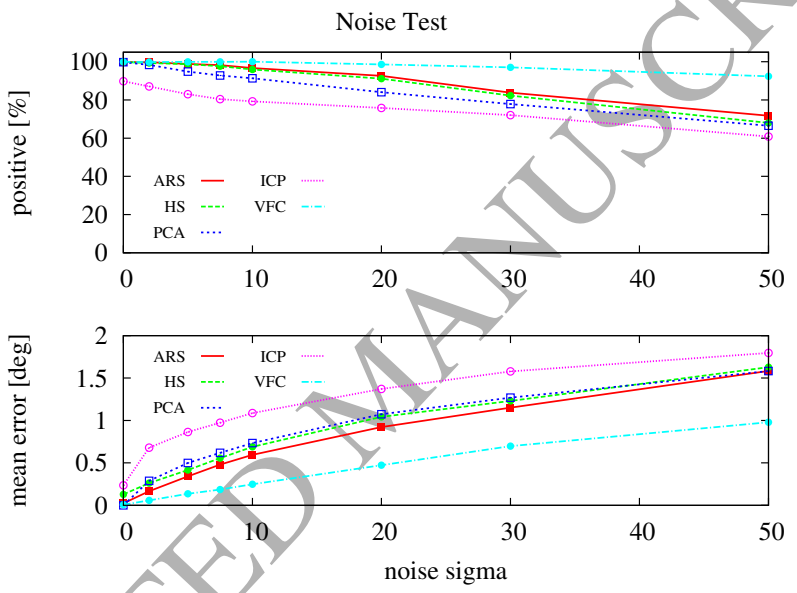

Figure 5: Positive estimation percentage (top) and mean angular error (bottom) obtained by ARS, HS and PCA methods by comparing point sets subject to different levels of Gaussian noise σ. A rotation estimation is positive if the rotation error is less than 5°. The mean angular error is computed only on positives.

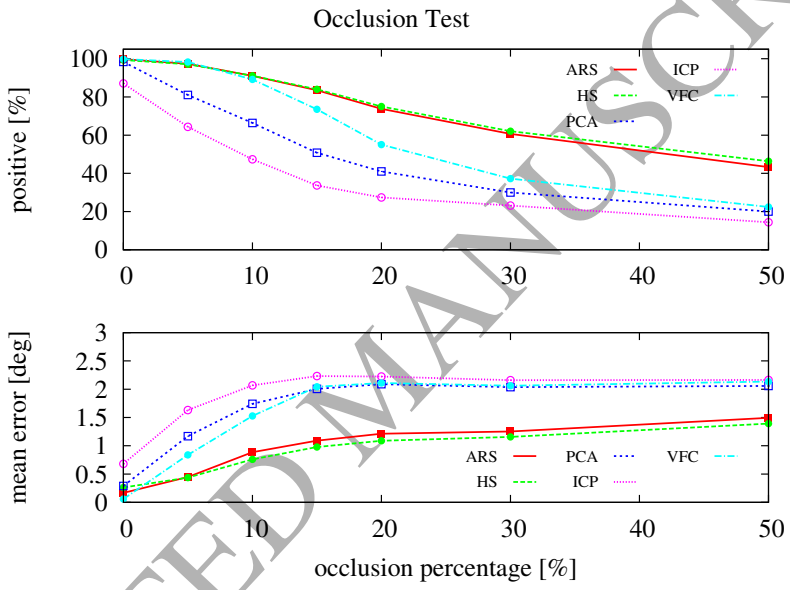

Figure 6: Positive estimation percentage (top) and mean angular error (bottom) obtained by ARS, HS and PCA methods by comparing point sets with different occlusion rates *beta* (in pencertage). A rotation estimation is positive if the rotation error is less than 5°. The mean angular error is computed only on positives.

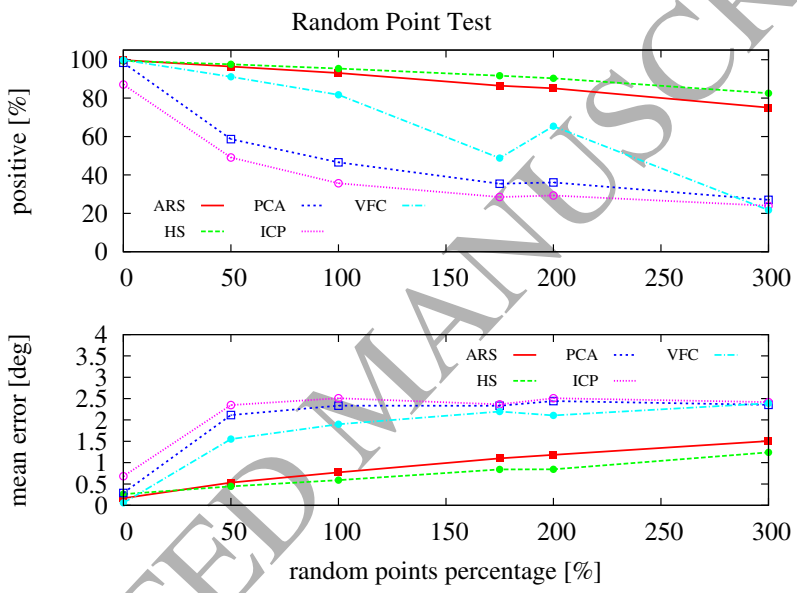

Figure 7: Positive estimation percentage (top) and mean angular error (bottom) obtained by ARS, HS and PCA methods by comparing point sets with different rates of random points γ (in percentage). A rotation estimation is positive if the rotation error is less than 5°. The mean angular error is computed only on positives.

category	ARS		HS		PCA		ICP		VFC	
	perc	err [°]	perc	err [°]	perc	err [°]	perc	err [°]	perc	err [°]
Bone	100	0.30	100	0.34	100	0.20	100	0.55	100	0.23
Comma	100	0.46	100	0.64	100	0.40	80	1.27	100	0.22
Glas	95	0.49	95	0.67	95	0.81	90	1.39	95	0.23
HCircle	100	0.88	100	1.18	100	0.75	85	1.59	100	0.30
Heart	100	0.76	100	0.70	95	0.76	90	1.25	100	0.21
Misk	100	0.64	100	0.83	95	1.08	90	1.34	100	0.19
apple	75	2.01	65	2.45	80	2.46	80	2.82	100	0.57
bat	100	0.26	100	0.34	100	0.30	85	0.42	100	0.13
beetle	100	0.72	100	0.76	95	0.90	85	1.15	100	0.32
bell	80	1.72	80	1.92	75	1.74	65	2.16	90	0.99
bird	100	0.58	100	0.73	100	0.62	70	0.94	100	0.36
bottle	95	1.54	95	1.63	95	1.37	90	1.28	95	1.09
brick	100	1.75	100	1.80	100	1.54	100	1.99	100	0.82
butterfly	100	0.56	100	0.64	100	0.79	80	1.17	100	0.24
camel	100	0.95	100	1.46	95	0.84	80	1.39	100	0.28
car	100	1.47	100	1.22	100	1.26	100	2.06	100	1.24
carriage	100	1.21	100	1.27	100	1.20	100	1.52	100	0.62
cattle	100	0.29	100	0.42	100	0.29	90	1.19	100	0.13
cellularphone	100	0.55	100	0.68	100	0.46	100	0.61	100	0.37
chicken	85	0.85	80	1.17	75	1.48	50	1.70	100	0.92
children	90	1.45	90	1.59	95	1.54	95	1.77	100	1.49
chopper	90	1.48	90	1.53	95	1.16	85	1.90	100	0.54
classic	100	0.51	100	0.59	100	0.44	100	0.71	100	0.19
crown	80	1.56	80	1.89	70	1.82	80	1.43	95	1.56
cup	100	1.53	95	1.94	80	2.79	80	2.59	100	0.28
deer	100	0.17	100	0.29	100	0.19	85	0.36	100	0.12
device0	70	0.25	75	0.45	25	2.16	10	1.67	100	0.16
device1	100	0.27	85	0.44	50	2.59	35	2.50	100	0.13
device2	55	0.56	55	0.77	10	1.15	10	1.65	100	0.20
device3	90	0.48	100	0.77	45	1.95	30	1.57	100	0.11
device4	100	0.40	100	0.42	55	2.04	35	2.07	100	0.18
device5	95	0.25	80	0.52	40	3.05	20	1.92	100	0.22
device6	100	1.09	95	1.17	65	1.74	65	2.18	100	0.18
device7	70	0.31	50	0.61	35	3.44	10	3.99	100	0.14
device8	100	0.28	100	0.46	55	2.58	25	1.87	100	0.20
device9	95	1.11	80	0.82	70	1.24	70	1.57	100	0.10
dog	95	0.82	95	1.02	95	0.85	95	1.12	100	0.34
elephant	95	0.54	95	0.69	100	0.74	90	0.81	100	0.25
face	100	1.59	100	2.10	100	1.34	100	1.42	100	0.29
fish	95	0.87	95	0.92	100	0.84	95	1.25	100	0.56
flatfish	100	0.86	100	1.10	100	0.48	100	0.82	100	0.31
fly	100	0.94	100	1.11	90	1.17	85	1.56	100	0.21
fork	100	0.47	100	0.59	100	0.42	70	1.18	100	0.25
fountain	85	1.53	85	1.32	30	3.03	10	0.83	100	0.58
frog	90	1.40	90	1.36	95	1.58	90	1.75	100	0.44
guitar	100	0.53	100	0.63	100	0.42	85	1.05	100	0.32
hammer	90	1.55	90	1.65	90	1.41	85	1.62	100	0.72
hat	75	1.92	60	1.50	60	1.57	55	1.71	95	1.13
horse	100	0.39	100	0.40	100	0.53	70	0.97	100	0.14
horseshoe	30	1.55	40	2.58	40	3.06	30	2.52	95	1.08
jar	100	1.07	95	1.36	100	0.61	95	1.00	100	0.22
key	100	0.78	100	0.70	100	0.76	100	0.93	100	0.61
lizzard	100	0.69	100	0.90	100	0.54	95	1.07	100	0.13
lmfish	100	0.80	95	0.70	100	0.71	95	0.99	100	0.50
octopus	85	1.71	85	1.94	45	1.85	40	1.23	100	0.50
pencil	100	0.63	100	0.63	100	0.55	100	1.01	100	0.59
personalcar	100	0.60	100	0.74	100	0.50	100	0.95	100	0.24
pocket	90	1.05	90	1.10	90	1.10	80	1.48	100	0.58
rat	90	2.07	95	2.30	95	1.68	70	2.09	95	0.54
ray	100	0.69	100	0.68	100	0.65	85	0.80	100	0.35
seasnake	95	0.79	100	1.16	95	0.74	90	1.41	100	0.81
shoe	100	0.73	100	0.95	100	0.53	100	0.84	100	0.28
spoon	95	0.83	95	0.83	95	0.81	95	1.37	95	0.72
spring	100	0.31	100	0.34	100	0.27	100	0.69	100	0.26
stef	55	2.69	50	2.72	60	2.38	35	1.95	65	2.03
teddy	85	2.25	75	1.83	55	3.09	70	3.40	100	0.39
tree	100	1.40	100	1.54	95	1.17	95	1.78	95	0.65
truck	70	1.93	60	2.09	65	1.74	65	2.28	85	2.07
turtle	100	1.03	100	1.23	100	0.88	90	1.55	100	0.39
watch	100	0.33	100	0.38	100	0.33	100	0.56	100	0.35

Table 1: Positive estimation percentage and mean angular error obtained by ARS, HS, PCA, ICP and VFC methods by different *shape categories* in **noise test** where Gaussian noise has standard deviation $\sigma = 20.0$.

category	ARS		HS		PCA		ICP		VFC	
	perc	err [°]	perc	err [°]	perc	err [°]	perc	err [°]	perc	err [°]
Bone	80	1.21	85	0.57	80	2.27	45	2.53	55	2.05
Comma	100	1.27	100	0.91	50	2.54	35	1.66	65	2.62
Glas	75	0.28	85	0.37	35	1.88	20	1.75	35	1.73
HCircle	95	0.29	95	0.25	40	2.78	25	2.55	30	2.66
Heart	90	1.02	100	1.10	15	1.89	15	3.53	40	1.79
Misk	95	1.24	100	0.84	5	4.79	10	1.41	45	2.84
apple	20	1.02	20	0.54	25	2.61	15	1.60	25	1.57
bat	80	0.79	70	0.86	45	2.27	35	2.02	55	1.85
beetle	65	1.44	70	1.37	15	2.70	15	2.49	40	1.33
bell	85	0.85	85	0.80	30	2.94	10	2.41	50	2.52
bird	65	1.32	70	1.48	40	2.23	30	2.81	50	1.82
bottle	100	1.41	100	1.43	100	1.75	65	1.88	65	2.20
brick	100	0.60	100	0.65	45	2.61	20	2.12	60	2.36
butterfly	55	2.00	45	1.69	15	2.10	5	1.21	25	2.57
camel	80	1.92	90	1.37	10	3.94	5	4.23	50	2.46
car	100	1.41	95	0.92	50	2.82	25	2.85	75	2.82
carriage	75	2.02	85	1.91	80	1.98	60	1.94	80	1.89
cattle	65	1.23	75	1.09	40	2.18	30	2.24	35	1.59
cellularphone	100	0.39	100	0.36	75	2.46	35	2.65	85	2.09
chicken	50	2.70	50	2.47	0	–	10	2.01	40	2.64
children	100	1.03	100	1.05	95	2.47	50	2.91	35	2.62
chopper	80	1.36	80	1.29	25	2.53	25	4.08	70	1.91
classic	95	1.35	95	1.12	90	2.09	65	2.80	95	1.76
crown	75	2.34	75	2.38	70	2.19	35	3.20	70	2.30
cup	80	1.26	75	1.07	15	1.58	15	3.04	60	2.30
deer	50	1.10	45	0.66	30	1.66	20	0.97	40	2.56
device0	15	0.05	20	0.19	0	–	0	–	65	1.81
device1	20	0.23	20	0.41	0	–	10	3.93	45	2.77
device2	55	0.13	45	0.15	5	2.64	10	1.21	50	2.34
device3	65	0.34	70	0.72	5	1.43	5	4.92	40	1.57
device4	45	0.94	55	0.88	10	2.55	10	1.66	20	0.94
device5	55	0.19	65	0.37	10	2.90	15	3.98	80	1.66
device6	55	0.80	60	0.89	5	0.62	0	–	30	2.18
device7	35	0.11	35	0.23	10	2.47	10	2.80	60	1.56
device8	85	0.70	75	0.53	15	2.85	15	2.16	50	2.18
device9	55	1.32	65	1.01	10	2.36	10	2.53	40	1.60
dog	60	2.59	45	1.92	35	2.25	15	2.37	45	2.97
elephant	70	1.44	55	1.45	45	2.38	35	2.72	60	2.01
face	70	1.48	70	1.50	35	2.49	25	3.89	35	2.57
fish	100	1.09	90	0.84	85	2.05	65	2.16	95	2.10
flatfish	85	1.48	90	1.37	65	1.96	40	1.49	80	2.10
fly	45	1.28	55	0.89	30	2.42	10	2.73	40	2.81
fork	95	1.48	100	0.95	80	1.71	55	1.59	65	1.57
fountain	55	1.56	70	1.43	0	–	0	–	40	2.83
frog	50	1.75	55	1.68	35	2.38	10	1.51	25	1.56
guitar	85	1.58	85	1.49	85	1.92	50	2.10	70	2.20
hammer	100	0.81	100	0.58	65	1.60	40	2.01	70	1.47
hat	85	1.28	85	1.36	30	2.97	15	1.09	40	1.49
horse	75	1.39	55	0.78	55	2.07	40	1.96	50	3.14
horseshoe	60	2.39	75	2.28	10	0.74	10	0.80	35	1.90
jar	95	1.42	85	1.26	35	1.72	30	3.53	50	2.24
key	95	1.68	100	1.33	75	2.15	45	1.95	85	2.15
lizzard	75	1.43	85	1.49	45	0.89	25	1.59	75	2.76
lmfish	100	0.92	100	0.77	90	1.56	70	2.24	90	2.08
octopus	45	1.31	45	1.46	0	–	5	1.88	45	2.08
pencil	100	0.39	100	0.30	100	0.92	95	1.32	100	0.77
personalcar	100	1.08	95	1.47	45	2.35	25	2.46	70	2.70
pocket	25	1.64	40	2.58	35	2.59	20	1.85	50	2.38
rat	70	2.12	75	1.79	50	2.06	25	2.74	65	2.04
ray	85	1.42	90	1.43	30	1.85	15	2.56	15	3.54
seasnake	100	1.34	100	1.29	55	1.97	45	2.47	60	2.36
shoe	95	0.72	90	0.54	60	2.34	35	1.84	75	1.85
spoon	95	1.51	95	1.45	85	1.78	50	1.86	85	2.32
spring	45	1.90	50	1.66	55	2.29	45	2.25	45	1.97
stef	55	1.71	50	1.57	40	2.26	25	2.41	50	1.66
teddy	55	1.42	55	1.27	0	–	5	1.07	30	2.56
tree	95	0.65	95	0.57	65	2.17	35	1.61	65	2.02
truck	75	1.83	80	1.14	45	3.01	20	2.31	55	3.00
turtle	85	1.47	90	1.20	20	1.73	15	3.43	45	2.33
watch	100	0.20	100	0.16	95	1.40	75	1.62	95	1.32

Table 2: Positive estimation percentage and mean angular error obtained by ARS, HS, PCA, ICP and VFC methods by different *shape categories* in **occlusion test** with occlusion rate equal to $\beta = 20\%$ of shape dimension.

category	ARS		HS		PCA		ICP		VFC	
	perc	err [°]	perc	err [°]	perc	err [°]	perc	err [°]	perc	err [°]
Bone	100	0.45	100	0.28	85	1.92	65	2.27	90	2.36
Comma	100	0.19	100	0.18	55	2.81	40	2.82	90	2.25
Glas	100	0.29	100	0.19	35	2.75	35	3.45	95	1.86
HCircle	100	0.21	100	0.21	50	1.92	40	2.12	75	1.88
Heart	95	0.37	100	0.33	20	3.45	5	2.44	100	1.71
Misk	95	1.17	95	0.47	20	1.60	20	1.51	90	1.58
apple	80	1.04	100	1.30	15	2.32	10	2.24	100	2.14
bat	100	0.30	100	0.25	80	1.97	65	2.90	95	1.86
beetle	100	0.74	100	0.64	55	2.36	45	2.93	85	2.07
bell	100	0.65	100	0.56	50	2.76	35	2.99	90	1.97
bird	100	1.12	100	0.61	65	2.74	50	2.68	85	2.01
bottle	100	0.47	100	0.36	60	3.31	30	2.73	60	1.74
brick	100	0.61	100	0.36	35	2.34	30	2.50	50	2.61
butterfly	100	0.95	100	0.72	60	2.30	55	2.66	60	1.70
camel	95	1.27	100	0.62	65	2.15	55	2.01	95	1.33
car	100	0.79	100	0.79	60	2.88	55	3.26	65	2.90
carriage	100	1.53	100	1.25	60	2.86	45	3.32	60	1.75
cattle	100	0.71	95	0.40	85	2.25	60	2.52	50	1.70
cellularphone	100	0.09	100	0.12	80	2.34	60	2.71	80	1.93
chicken	80	0.95	85	1.11	30	1.96	25	2.73	85	1.83
children	100	0.84	100	0.62	45	2.89	25	3.50	55	2.70
chopper	100	1.19	100	0.76	50	3.08	15	1.79	75	1.53
classic	100	0.47	100	0.30	65	2.30	55	2.90	80	1.75
crown	90	1.68	90	1.49	30	2.01	25	1.49	55	2.52
cup	100	0.31	100	0.31	10	2.83	5	0.54	100	1.45
deer	100	0.54	100	0.40	100	1.85	90	2.62	25	2.38
device0	70	0.20	75	0.26	10	1.89	10	3.02	95	1.73
device1	55	0.13	75	0.19	20	1.56	20	2.70	100	2.04
device2	60	0.16	70	0.17	0	–	0	–	95	1.51
device3	80	0.16	95	0.14	10	3.76	5	2.77	100	0.65
device4	100	0.10	100	0.15	15	0.93	15	1.95	100	2.07
device5	85	0.23	95	0.13	15	1.90	10	0.36	90	1.64
device6	95	0.27	95	0.20	25	2.21	25	2.67	90	1.57
device7	15	0.12	45	0.11	5	1.51	5	2.80	90	1.54
device8	100	0.17	100	0.19	0	–	0	–	85	1.65
device9	90	0.58	85	0.18	25	2.39	25	2.15	95	1.36
dog	95	0.92	95	0.77	70	2.31	50	2.59	70	1.95
elephant	100	0.63	100	0.31	70	2.49	55	2.48	100	1.67
face	100	1.30	100	0.86	30	2.53	35	3.10	75	1.64
fish	100	0.74	100	0.52	55	2.39	30	1.88	80	2.36
flatfish	95	1.67	95	0.74	35	2.34	25	2.06	75	2.47
fly	100	0.82	100	0.55	60	2.54	45	2.80	95	2.39
fork	100	0.24	100	0.13	85	2.16	65	1.96	95	2.15
fountain	100	0.77	100	0.77	5	3.53	0	–	80	1.91
frog	100	1.44	100	1.28	55	1.65	50	2.56	95	2.41
guitar	100	0.60	100	0.33	70	1.95	55	2.50	70	2.09
hammer	100	0.38	100	0.32	55	2.15	50	1.88	75	2.11
hat	80	0.62	85	0.71	35	3.06	25	3.39	90	2.95
horse	100	0.81	100	0.59	70	2.05	55	2.40	95	1.87
horseshoe	70	1.53	70	1.60	10	1.59	15	2.66	85	1.60
jar	100	1.12	100	0.56	55	2.85	30	2.49	100	1.16
key	100	0.81	100	0.47	40	3.15	20	3.48	80	2.65
lizzard	100	1.12	100	0.86	85	2.38	65	2.50	90	1.53
lmfish	100	0.59	100	0.43	65	2.58	45	2.69	70	1.65
octopus	55	2.08	70	1.89	15	1.96	5	0.39	90	2.14
pencil	100	0.16	100	0.19	60	2.69	30	2.70	75	2.30
personalcar	100	0.50	100	0.34	65	2.91	40	2.40	80	2.54
pocket	85	1.87	90	1.75	30	2.61	30	1.98	70	2.59
rat	100	1.60	100	1.34	50	2.02	45	1.78	95	1.68
ray	100	0.97	100	0.39	60	2.70	30	1.86	90	1.55
seasnake	95	0.81	100	0.69	55	2.09	45	2.47	100	1.79
shoe	100	0.54	100	0.29	75	2.43	55	2.90	85	1.83
spoon	100	0.55	100	0.46	70	1.81	65	2.22	65	2.27
spring	100	0.53	100	0.43	100	1.44	95	2.30	95	1.24
stef	80	1.84	80	1.65	35	2.73	25	1.78	65	1.92
teddy	85	1.05	95	0.99	20	3.64	15	4.68	90	1.69
tree	95	1.05	95	0.67	30	2.26	20	2.39	70	2.28
truck	95	2.23	100	1.83	35	1.26	35	2.19	70	2.00
turtle	100	0.90	100	0.60	60	2.41	50	2.86	95	1.89
watch	100	0.18	100	0.14	60	1.84	40	1.55	35	1.44

Table 3: Positive estimation percentage and mean angular error obtained by ARS, HS, PCA, ICP and VFC methods by different *shape categories* in **random point test** with random point rate $\gamma = 100\%$.

algorithm	average time [ms]
ARS	794.8
HS	18.3
PCA	8.8
ICP	12.3
VFC	69.2

Table 4: Average execution time of algorithms on 1400 shapes of MPEG-7 dataset. The average number of points per shape is 1443.8.